Chapter 1

Conical Intersections in Organic Photochemistry

Michael A. Robb*

*Chemistry Department, Imperial College London, London SW7 2AZ, UK.

1. Introduction

It has now been about 20 years[1] since we published our first paper on a conical intersection in the prototypical organic photochemical problem: the $2+2$ face-to-face cycloaddition of two ethylenes. In the intervening period, conical intersections have become an essential part of the thought process or paradigm of organic photochemistry (see, for example, the textbooks of Klessinger[2] or Turro[3]). In the previous volume of this series on conical intersections, Migani and Olivucci[4] not only have given an extensive review of the history of the subject and the theory of conical intersections associated with the mechanisms of organic photochemistry, but also discussed many examples that cover the complete range of functional groups that are important in organic photochemistry. The subject is now growing so rapidly that to simply update the Migani article with the photochemical problems that have been studied in the last five years would be almost impossible within the space allowed (but see recent reviews[5−7]). Rather, we limit our discussion to those areas identified by Migani and Olivucci as areas of major growth into the future. These areas include the relationship between the intersection space or the conical intersection seam and photochemical mechanisms, the use of dynamics to investigate organic photochemistry, and the extension to biological chromophores. In addition to these topics, we shall discuss a little about the use of qualitative methods to rationalise computations because this area remains important for the organic chemist.

In writing this section, our target was to produce a more general discussion that seemed to be appropriate for a section focussed on "fundamental aspects". Thus the intention was to be rather broad with most of the examples chosen (mainly from our own work) so as to illustrate conceptual ideas. In the examples, we will choose to discuss the concepts, we will omit the computational details and refer the reader to the original literature. In general, the results are from the CASSCF method where both gradients

and hessian can be computed analytically so that we do not need to use "distinguished variables" but rather full geometry optimization is possible. Since most of our discussions are focussed on the general shape of the potential surface near a conical intersection, there is not a requirement for high accuracy.

2. Exploring the Intersection Space: The Extended Conical Intersection Seam

2.1. *Theory*

It is our intention in this section to discuss the mechanistic implications of the extended conical intersection seam.[7–16] We start with a theoretical discussion adapted from the work of Sicila and co-workers.[15]

One often starts a discussion of conical intersections in organic photochemistry with "sand in a funnel" picture for a photochemical mechanism involving excited and ground state branches (with two ground state reaction pathways) and a conical intersection (Fig. 1). We shall use cartoons of this form to illustrate many aspects of nonadiabatic chemistry in this article.

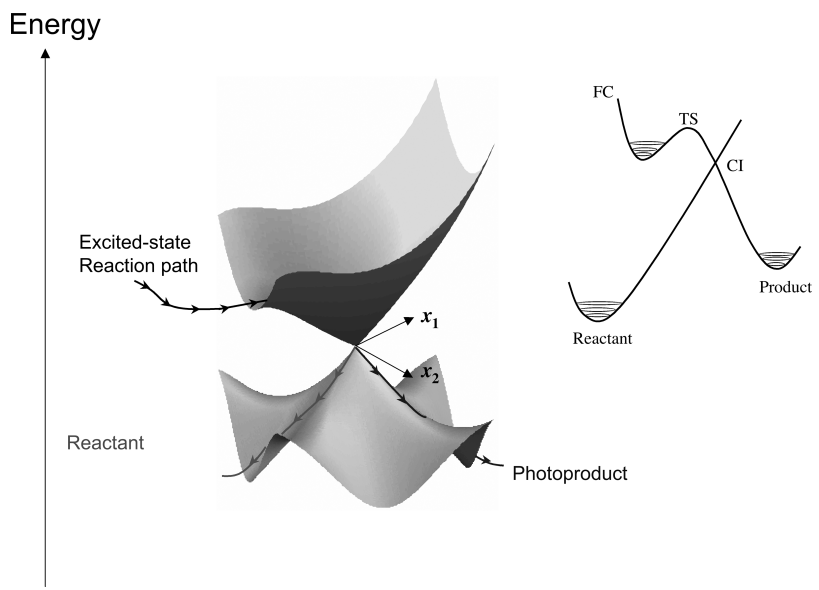

Fig. 1. Cartoon of a "classic" double cone conical intersection, showing the excited-state reaction path and two ground-state reaction paths. (Adapted from Paterson *et al.*[12])

We begin by offering a few comments on how such cartoons should be interpreted. We have plotted the energy in two geometrical coordinates, X_1 and X_2. In general, these two coordinates will be combinations of changes in the bond lengths and bond angles of the molecular species under investigation. We are limited in such cartoons to using two or three combinations of molecular variables. However, we must emphasise that these are just cartoons used to illustrate a mechanistic idea. All the computations we shall discuss are done in the full space of molecular geometries without any constraint.

The coordinates X_1 and X_2 in Fig. 1 correspond to the space of molecular geometrical deformations that lift the degeneracy. These coordinates are precisely defined quantities that can be computed explicitly.[17] Similarly, the apex of the cone corresponds in general to an optimised molecular geometry.[18] (See also the more recent work of Sicila,[13] Martinez[19] and Theil.[20]) The shape or topology in the region of the apex of the double cone will change from one photochemical system to another,[9] and it is the generalities associated with the shape that form part of the mechanistic scenario that we will discuss.

Conical intersections are normally thought of as points on a $(m-2)$-dimensional hyperline. While the degeneracy is lifted by motion in branching space X_1 and X_2 in Fig. 1, motions in the intersection space X_3 shown in Fig. 2 preserve the degeneracy. Thus in Fig. 2, we show the conical intersection hyperline traced out by a coordinate X_3 plotted, this time, in a plane containing the distinguished intersection space coordinate X_3 and one coordinate from the degeneracy-lifting (or branching) space X_1 X_2. We shall call X_3 the "reaction coordinate" because this might be chosen as the path of steepest decent on the potential surface and this would be a gradient-determined choice of this distinguished coordinate. In this figure, the conical intersection line now appears as a seam. In contrast to the "sand in the funnel" model shown in Fig. 1, it is clear that the reaction path could be almost parallel to this seam. Of course this figure can be misunderstood, because each point on the seam line lies in the space of the double-cone X_1 X_2 as suggested by the insert. Thus it is essential to appreciate that decay at the conical intersection is associated with three coordinates, the branching space X_1 X_2 and the reaction path X_3 that may or may not lie in the space X_1 X_2.

In Fig. 3, we have presented another cartoon that attempts to show the potential energy surfaces in the space of the degeneracy lifting coordinates as one traverses a third coordinate X_3. Of course, this is really

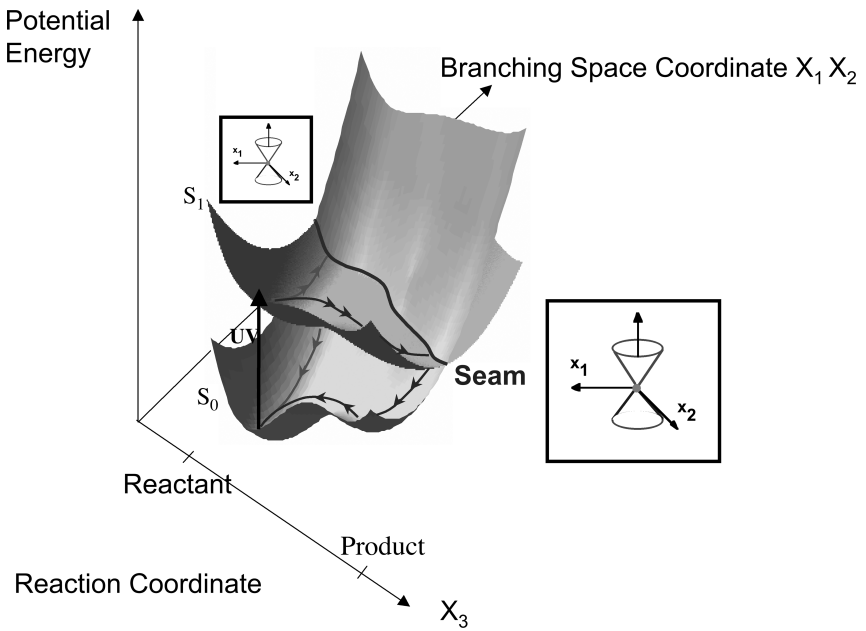

Fig. 2. The conical intersection hyperline traced out by a coordinate X_3 plotted in a space containing the coordinate X_3 and one coordinate from the degeneracy-lifting space X_1 X_2. (Adapted from Paterson *et al.*[12])

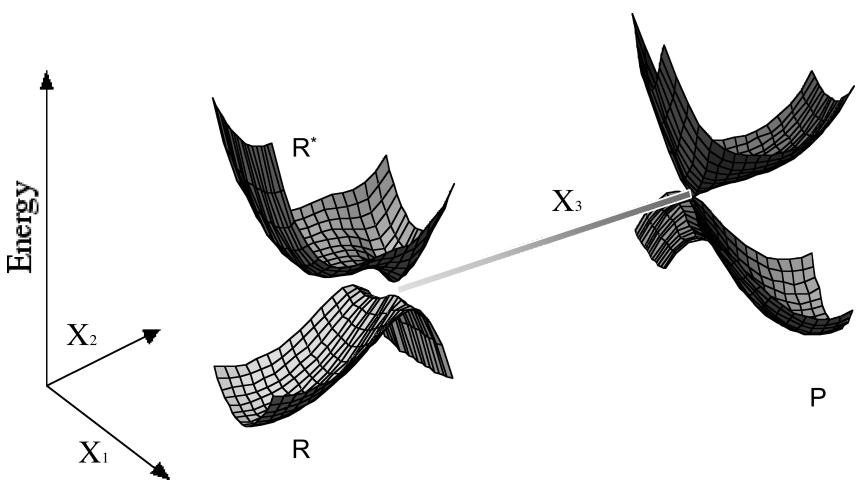

Fig. 3. A cartoon showing the conical intersection hyperline traced out by a degeneracy-preserving coordinate X_3. The system remains degenerate as one traverses the coordinate X_3, but the energy and the shape of the double-cone must change in X_1X_2.

a four-dimensional picture, which is not easy to assimilate. Nevertheless it should be clear that the degeneracy persists along the coordinate X_3. However, the energy will change and so will the "shape" of the double-cone near the apex.

Figures 2 and 3 establish two important mechanistic points:

(1) The important points on a conical intersection hyperline are those where the reaction path meets with the seam (see Fig. 2) and this may not be at the minimum of the seam.
(2) Radiationless decay takes place in the coordinates X_1 X_2 as one passes through the conical intersection diabatically.

In Fig. 2, this second principle appears to be violated since the reaction path appears to pass through the hyperline adiabatically. However, we emphasise — as indicated by the double-cone insert — that as one passes through the hyperline, decay takes place in the coordinates X_1 X_2 and in general their VB structure does not change. We shall use both Figs. 2 and 3 as models in subsequent discussions, but the reader needs to remember the conceptual limitations.

The statement that motion in the intersection space preserves the degeneracy is only true to first order and, in fact, the degeneracy can be lifted at second order by finite steps along coordinates spanning the intersection space. We now develop this idea and show that it can be used to further characterise conical intersections (for further details, the reader is referred to the literature[9−16]).

A second-order description of conical intersections allows one to characterise optimised conical intersection geometries as either minima or saddle points on the crossing hyperline. We will now present[15] a simplified development of the second-order description of conical intersections. However, first we briefly introduce the ideas behind such description in a nonmathematical way with the aid of Fig. 4. In numerical computations, one finds that the degeneracy is, in practice, lifted for a finite displacement along any intersection space coordinate (X_3 in Fig. 2 and Q_i in Fig. 4). Figure 4(a) shows a minimum on the extended seam while Fig. 4(b) shows a saddle point. The curve f_i corresponds to the projection of the seam $U(f_i)$ on the coordinate space consisting of one coordinate from the branching plane, $\bar{Q}_{x_{12}}$, and one from the intersection space, $\bar{Q}_i$. Thus, the crossing seam is curved so that the seam bends towards the branching plane coordinate, with a mixing of branching space and intersection space coordinates. This

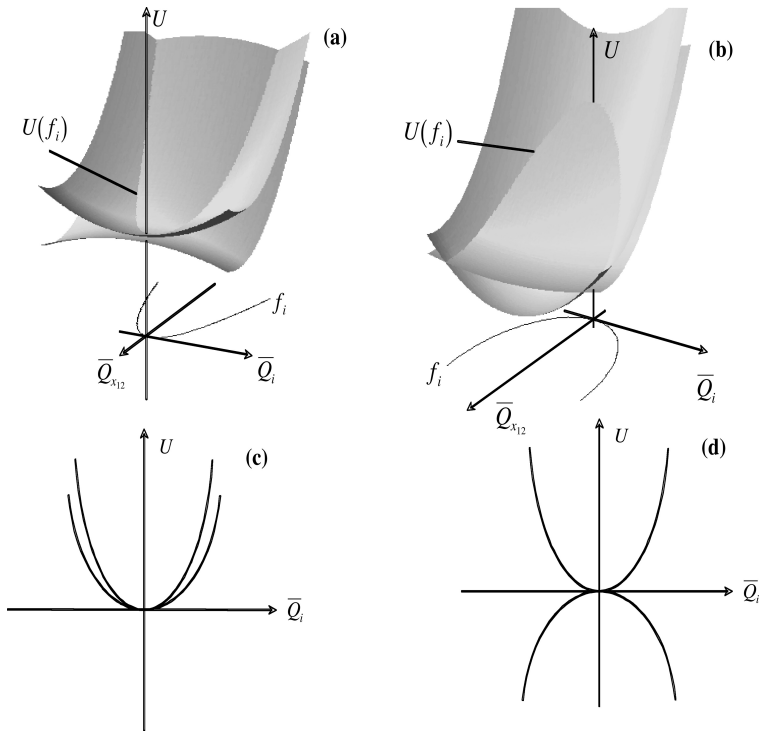

Fig. 4. The locus of the conical intersection seam $U(f_i)$ and the corresponding curvilinear coordinate f_i: (a) minimum, (b) saddle point, (c) cross section of (a) along first-order intersection space coordinate $\bar{Q}_i$, and (d) cross section of (b) along first-order intersection space coordinate $\bar{Q}_i$. (Adapted from Sicilia *et al.*[15])

curvature is required to describe finite displacements where the degeneracy is preserved.

In Figs. 4(c) and 4(d) we show cuts through Figs. 4(a) and 4(b) in the $(U,\ \bar{Q}_i)$ plane. It is clear in this figure that the two potential energy curves split apart along any finite displacement lying strictly along the rectilinear first-order intersection modes, $\bar{Q}_i$, that is in the plane containing energy and the intersection coordinate.

Figure 4 shows that a curvilinear coordinate f_i is a convenient way to describe the behaviour of the extended seam. If we define the curvilinear coordinates as f_i, the crossing seam energy can be written as a function of these $(m-2)$ variables $U(f_i)$ rather than the $(m-2)$ rectilinear coordinates. It then becomes clear that the curvature of the seam energy becomes simply

the second derivative of the seam energy with respect to such curvilinear coordinates. We will refer to the matrix of second derivatives computed in this way as the intersection space Hessian. The curvilinear coordinates just discussed are the second-order generalization of the intersection-adapted coordinates introduced by Atchity *et al.*[9]

We now proceed to a more mathematical discussion.[15] We begin with a first order description of a conical intersection. The first-order approximation describes the two intersecting potential energy surfaces in the vicinity of a conical intersection point. In an appropriate region around the intersection point, the electronic two-state potential energy matrix describing the two intersecting *states* A and B can be approximated by a Taylor expansion truncated at the second order[21]:

$$\mathbf{W} = \mathbf{W}^{(0)} + \mathbf{W}^{(1)} + \frac{1}{2}\left\{\mathbf{W}_a^{(2)} + 2\mathbf{W}_b^{(2)} + \mathbf{W}_c^{(2)}\right\}. \tag{1}$$

The reference point is assumed to be the conical intersection point. Therefore, the zero-order term $\mathbf{W}^{(0)}$ is a diagonal matrix whose entries are equal; in the following this matrix is set to zero. When the expansion is performed with respect to the m first-order intersection adapted coordinates $\bar{Q}_i$, the potential matrices can be explicitly written as:

$$\mathbf{W}^{(1)} = \left(\frac{\lambda_1}{2}\bar{Q}_{x_1} + \frac{\lambda_2}{2}\bar{Q}_{x_2}\right)\mathbf{1} + \begin{pmatrix} \frac{\delta\kappa}{2}\bar{Q}_{x_1} & \kappa^{AB}\bar{Q}_{x_2} \\ \kappa^{AB}\bar{Q}_{x_2} & -\frac{\delta\kappa}{2}\bar{Q}_{x_1} \end{pmatrix}, \tag{2a}$$

$$\mathbf{W}_a^{(2)} = \left(\sum_{i,j\in BS} \frac{{}^{BS}\omega_{ij}}{2}\bar{Q}_i\bar{Q}_j\right)\mathbf{1} + \begin{pmatrix} \sum_{i,j\in BS} \frac{{}^{BS}\delta\gamma_{ij}}{2}\bar{Q}_i\bar{Q}_j & \sum_{i,j\in BS} {}^{BS}\eta_{ij}^{AB}\bar{Q}_i\bar{Q}_j \\ \sum_{i,j\in BS} {}^{BS}\eta_{ij}^{AB}\bar{Q}_i\bar{Q}_j & -\sum_{i,j\in BS} \frac{{}^{BS}\delta\gamma_{ij}}{2}\bar{Q}_i\bar{Q}_j \end{pmatrix}, \tag{2b}$$

$$\mathbf{W}_b^{(2)} = \left(\sum_{i\in BS, j\in IS} \frac{{}^{BS/IS}\omega_{ij}}{2}\bar{Q}_i\bar{Q}_j\right)\mathbf{1}$$

$$+\begin{pmatrix} \sum_{i\in BS,j\in IS} \frac{^{BS/IS}\delta\gamma_{ij}}{2}\bar{Q}_i\bar{Q}_j & \sum_{i\in BS,j\in IS} {}^{BS/IS}\eta_{ij}^{AB}\bar{Q}_i\bar{Q}_j \\ \sum_{i\in BS,j\in IS} {}^{BS/IS}\eta_{ij}^{AB}\bar{Q}_i\bar{Q}_j & -\sum_{i\in BS,j\in IS} \frac{^{BS/IS}\delta\gamma_{ij}}{2}\bar{Q}_i\bar{Q}_j \end{pmatrix}, \tag{2c}$$

$$\mathbf{W}_c^{(2)} = \left(\sum_{i,j\in IS} \frac{^{IS}\omega_{ij}}{2}\bar{Q}_i\bar{Q}_j\right)\mathbf{1}$$

$$+\begin{pmatrix} \sum_{i,j\in IS} \frac{^{IS}\delta\gamma_{ij}}{2}\bar{Q}_i\bar{Q}_j & \sum_{i,j\in IS} {}^{IS}\eta_{ij}^{AB}\bar{Q}_i\bar{Q}_j \\ \sum_{i,j\in IS} {}^{IS}\eta_{ij}^{AB}\bar{Q}_i\bar{Q}_j & -\sum_{i,j\in IS} \frac{^{IS}\delta\gamma_{ij}}{2}\bar{Q}_i\bar{Q}_j \end{pmatrix}. \tag{2d}$$

In the above equations, the potential constants are defined as:

$$\lambda_i \equiv \nabla_{\bar{Q}_{x_i}}(U_{AA}^0 + U_{BB}^0), \tag{3a}$$

$$\delta\kappa \equiv \nabla_{\bar{Q}_{x_1}}(U_{BB}^0 - U_{AA}^0), \tag{3b}$$

$$\kappa^{AB} \equiv \nabla_{\bar{Q}_{x_2}} H_{AB}^0, \tag{3c}$$

$$\omega_{ij} \equiv \nabla^2_{\bar{Q}_i\bar{Q}_j}(U_{AA}^0 + U_{BB}^0), \tag{3d}$$

$$\delta\gamma_{ij} \equiv \nabla^2_{\bar{Q}_i\bar{Q}_j}(U_{BB}^0 - U_{AA}^0), \tag{3e}$$

$$\eta_{ij}^{AB} \equiv \nabla^2_{\bar{Q}_i\bar{Q}_j} H_{AB}^0. \tag{3f}$$

In Eq. (3), we use the nabla, ∇, to indicate the vector differential operator of first derivatives with respect to nuclear displacements. Therefore, when applied to a scalar, it will give rise to a vector. In the context discussed here, it indicates exclusively the gradient vector. The subscript is introduced to specify which component of the entire vector is considered. Thus, for instance, the element of the gradient calculated with respect to the $\hat{\mathbf{x}}_i$ direction is indicated as ∇_{Q_i}. Note the equivalence $\nabla_{Q_i} \equiv \partial/\partial\bar{Q}_i$. Nabla squared, ∇^2, is an extension of such notation and, therefore, its application to a scalar gives rise to a square symmetrical matrix whose elements are defined as $\nabla^2_{\bar{Q}_i\bar{Q}_j} \equiv \partial^2/(\partial\bar{Q}_i\partial\bar{Q}_j)$. The zero superscripts indicate that all the terms are computed at the reference point (a critical point on the seam).

We now introduce the parabolic approximation where the second-order terms within the first-order branching space ${}^{BS}\delta\gamma_{ij}$ and ${}^{BS}\eta_{ij}^{AB}$, and the mixing terms between branching plane and first-order intersection space ${}^{BS/IS}\delta\gamma_{ij}$ and ${}^{BS/IS}\eta_{ij}^{AB}$, are neglected (the parabolic approximation derives from a three-dimensional case where the approximate intersection coordinate moves along a parabola). In the parabolic approximation, we are left with a simplified electronic Hamiltonian that can be written as:

$$\mathbf{W} = \left(\frac{\lambda_1}{2}\bar{Q}_{x_1} + \frac{\lambda_2}{2}\bar{Q}_{x_2} + \sum_{i,j\in IS} \frac{{}^{IS}\omega_{ij}}{4}\bar{Q}_i\bar{Q}_j \right) \mathbf{1} + \begin{pmatrix} \frac{\delta\kappa}{2}\bar{Q}_{x_1} & \kappa^{AB}\bar{Q}_{x_2} \\ \kappa^{AB}\bar{Q}_{x_2} & -\frac{\delta\kappa}{2}\bar{Q}_{x_1} \end{pmatrix} + \begin{pmatrix} \sum_{i,j\in IS} \frac{{}^{IS}\delta\gamma_{ij}}{4}\bar{Q}_i\bar{Q}_j & \sum_{i,j\in IS} \frac{{}^{IS}\eta_{ij}^{AB}}{2}\bar{Q}_i\bar{Q}_j \\ \sum_{i,j\in IS} \frac{{}^{IS}\eta_{ij}^{AB}}{2}\bar{Q}_i\bar{Q}_j & -\sum_{i,j\in IS} \frac{{}^{IS}\delta\gamma_{ij}}{4}\bar{Q}_i\bar{Q}_j \end{pmatrix}. \tag{4}$$

The description of two adiabatic potential energy surfaces around the conical intersection point is obtained from the diagonalisation of the simplified electronic Hamiltonian to give:

$$U_{A,B} = \frac{1}{2}\left\{ \lambda_{x_1}\bar{Q}_{x_1} + \lambda_{x_2}\bar{Q}_{x_2} + \sum_{i,j\in IS} \frac{{}^{IS}\omega_{ij}}{2}\bar{Q}_i\bar{Q}_j \right\} \pm \frac{1}{2}\sqrt{\left[\delta\kappa\bar{Q}_{x_1} + \sum_{i,j\in IS} \frac{{}^{IS}\delta\gamma_{ij}}{2}\bar{Q}_i\bar{Q}_j \right]^2 + 4\left[\kappa^{AB}\bar{Q}_{x_2} + \sum_{i,j\in IS} \frac{{}^{IS}\eta_{ij}^{AB}}{2}\bar{Q}_i\bar{Q}_j \right]^2}. \tag{5}$$

Thus the positive energy difference between the two states is:

$$\Delta U \equiv U_B - U_A = \sqrt{\left[\delta\kappa\bar{Q}_{x_1} + \sum_{i,j\in IS} \frac{{}^{IS}\delta\gamma_{ij}}{2}\bar{Q}_i\bar{Q}_j \right]^2 + 4\left[\kappa^{AB}\bar{Q}_{x_2} + \sum_{i,j\in IS} \frac{{}^{IS}\eta_{ij}^{AB}}{2}\bar{Q}_i\bar{Q}_j \right]^2}. \tag{6}$$

The two coordinates describing the branching space in the parabolic approximation will be a combination of first-order intersection adapted coordinates

such that the energy difference Eq. (6) does not vanish. The remaining $(m-2)$ parabolic intersection coordinates will be a set of coordinates where the two intersecting states possess the same energy. This is possible by identifying a set of parameters for which the energy difference Eq. (6) is zero.

Thus the set of curvilinear coordinates f is defined as:

$$f = (f_1, f_2) \oplus (f_3, f_4, \ldots, f_{m-2}). \tag{7}$$

The first bracket includes the two coordinates spanning the parabolic branching space and using the description of the energy difference; these two coordinates may be explicitly defined as:

$$f_1 = \delta\kappa\bar{Q}_{x_1} + \sum_{i,j\in IS} \frac{^{IS}\delta\gamma_{ij}}{2}\bar{Q}_i\bar{Q}_j, \tag{8a}$$

$$f_2 = \kappa^{AB}\bar{Q}_{x_2} + \sum_{i,j\in IS} \frac{^{IS}\eta_{ij}^{AB}}{2}\bar{Q}_i\bar{Q}_j. \tag{8b}$$

The second subset of coordinates corresponds to the $(m-2)$ parabolic intersection coordinates, which are a combination of the original coordinates where the following conditions are simultaneously fulfilled:

$$\begin{cases} f_1 = 0 \\ f_2 = 0. \end{cases} \tag{9}$$

When moving along one of the first two coordinates (f_1, f_2), the degeneracy is lifted whilst a displacement along the third f_3 guarantees the degeneracy between the two states. The seam hessian can now be written[15] in these parabolic intersection space coordinates as

$$\left.\frac{\partial^2 U_{Seam}}{\partial f^2}\right|_{\mathbf{f}=0} = \begin{bmatrix} \nu_{33} & \nu_{34} & \cdots & \nu_{3,3N-6} \\ \nu_{34} & \nu_{44} & \cdots & \nu_{4,3N-6} \\ \vdots & \vdots & \ddots & \vdots \\ \nu_{3,3N-6} & \nu_{4,3N-6} & \cdots & \nu_{3N-6,3N-6} \end{bmatrix}, \tag{10}$$

where an arbitrary entry ν_{ij} can be rewritten in terms of potential constants as:

$$\nu_{ij} = \frac{1}{2}\left(^{IS}\omega_{ij} - \frac{\lambda_{x_1}}{\delta\kappa}{}^{IS}\delta\gamma_{ij} - \frac{\lambda_{x_2}}{\kappa^{AB}}{}^{IS}\eta_{ij}^{AB}\right). \tag{11}$$

The curvature of the seam along the i-th coordinate is the i-th eigenvalue of the matrix [Eq. (11)]. All the matrix entries and eigenvalues have units of frequency squared; in atomic units this corresponds to s^{-2}. The eigenvectors obtained by diagonalisation of Eq. (11) are a combination of the $(m-2)$ local axes $\hat{\mathbf{f}}_i$, $i = 3, 4, \ldots, m-2$, tangent to the f_i at a given point.

We now discuss some benchmark applications of the theoretical ideas just presented.

3. Extended Seam Benchmarks

3.1. *Fulvene*

Fulene seems to have become a benchmark molecule for the study of conical intersections.[16,22] In recent work,[16] we have been able to optimise five geometries on an extended conical intersection seam so this provides a nice example to illustrate the theoretical ideas about the extended seam discussed in the preceding subsection.

A schematic two-dimensional schematic potential energy surface is given in Fig. 5. The branching space coordinates are given in the inset of Fig. 5 and correspond to the skeletal deformations of the five-membered ring. So we choose one of these skeletal deformations as $\bar{Q}_{x_1}$ in Fig. 5, while a suitable choice for a reaction coordinate $\bar{Q}_{x_3}$ is the torsional angle $\bar{Q}_{\phi}$. In Fig. 5 we can see that the extended curve has both a local maxima at a geometry we call $\mathrm{CI}_{\mathrm{perp}}$ and a minimum at a twisted geometry. However, the situation is more complicated as one goes to higher dimensions. In fact, $\mathrm{CI}_{\mathrm{perp}}$ is a second-order saddle point on the seam with two imagining frequencies corresponding to torsion and pyramidalisation (see the imaginary frequencies illustrated on the left-hand side of the Fig. 5). However, even after a distortion along a pyramidalisation coordinate, the structure $\mathrm{CI}_{\mathrm{pym}}$ retains the imaginary frequency corresponding to torsion.

The full set of stationary points on the conical intersection seam, excluding $\mathrm{CI}_{\mathrm{perp}}$, is given in Fig. 6 together with the computed imaginary frequencies in the intersection space. The structure $\mathrm{CI}_{\mathrm{plan}}$ is a second-order saddle point (like $\mathrm{CI}_{\mathrm{perp}}$) and is unstable with respect to both torsion and pyramidalisation. The pyramidalised structure $\mathrm{CI}_{\mathrm{pym}}$ is a saddle point

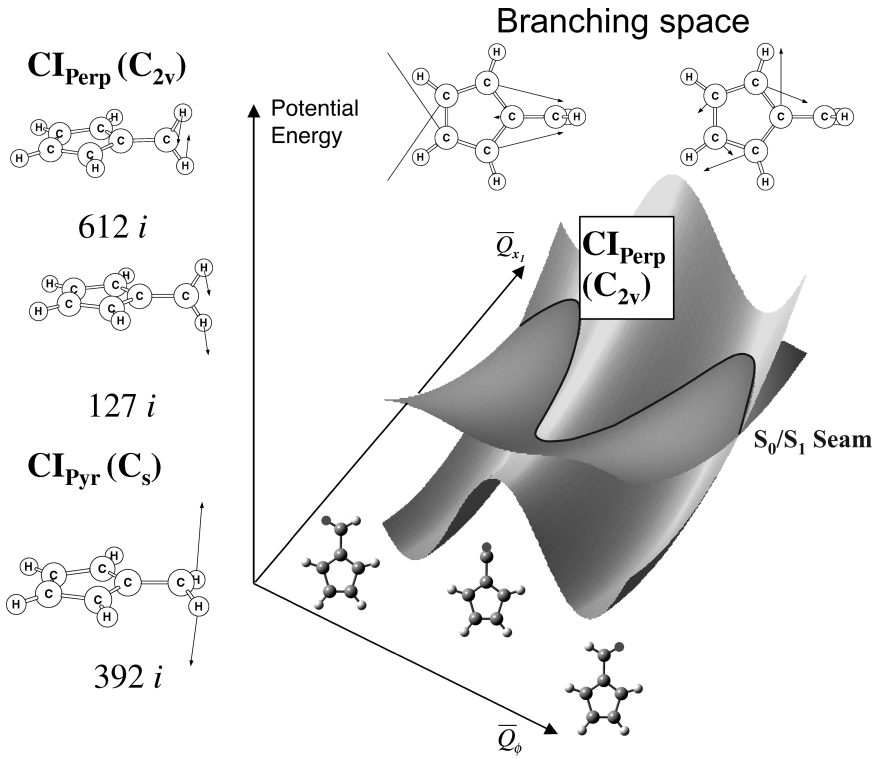

Fig. 5. Potential energy profile for fulvene in the space spanned by Q_{X1} (branching space) and Q_ϕ the X_3 coordinate (torsion). (Adapted from Paterson *et al.*[11])

with respect to torsion that leads to the partly twisted structure CI_{min}. In contrast, if one follows the torsional coordinate from CI_{plan}, one reaches a structure that is twisted but not pyramidalised that is denoted as CI_{63}.

Of course such a study of the full seam is just an academic exercise. *A posteriori* results seem obvious. Along the seam the energies of excited and ground state are equal. Thus the electronic effects associated with the π system are in balance. This leads to the conclusion that the stability with respect to torsion is a steric affect. Similarly, the stability with respect to pyramidalisation is the simply expected stereochemistry of an isolated methylene group.

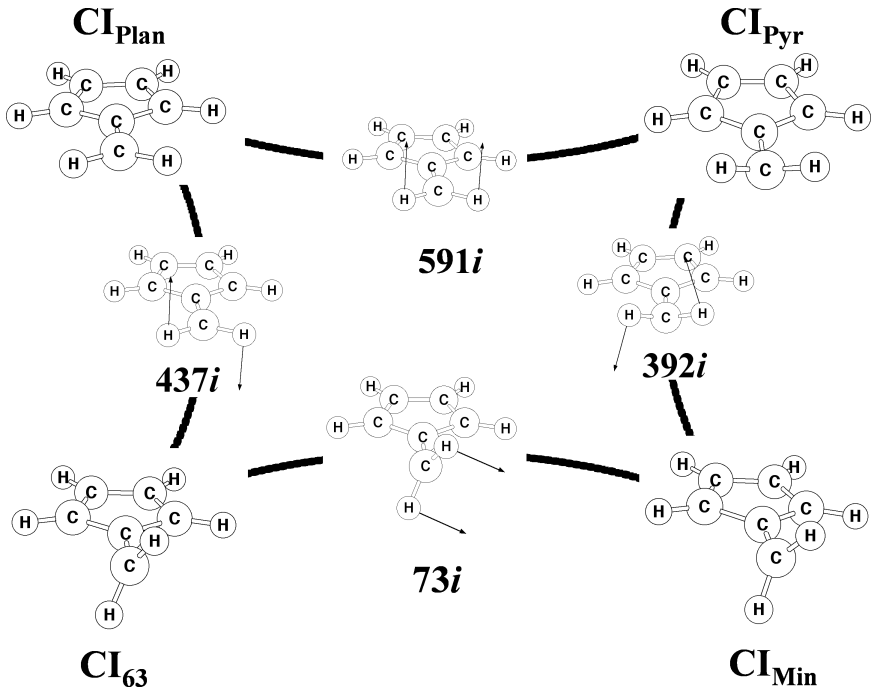

Fig. 6. Schematic representation of the conical intersection hyperline topology (excluding $\mathbf{CI}_{\mathrm{Perp}}$) in the space of torsion and pyramidalisation. The seam normal modes corresponding to the imaginary frequencies that connect the conical intersection geometries optimised on the S_0/S_1 seam of fulvene are shown as vectors for hydrogen motions only. (Adapted from Sicilia *et al.*[16])

3.2. *The $2A_1/1A_1$ conical intersection seam in butadiene*

This is another benchmark type problem. While initial photoexcitation takes place at the optically bright B state, the photochemistry of cis-butadiene (Fig. 7) occurs via a conical intersection between the $2A_1$ state and the ground state. Photolysis yields many products, possibly from decay at different points on the seam; the results are summarised in Fig. 7.

Some seven critical points[13,15] on the seam are illustrated in Fig. 8. In our early work,[23] we located CI_{cis}, $^{sp}CI_{cis/trans}$ and CI_{trans}. In Fig. 7, we see that $^{sp}CI_{cis/trans}$ is confirmed as a saddle point. In fact, it has been possible to use reaction path procedure,[13] constrained to the intersection space, to connect all these structures.

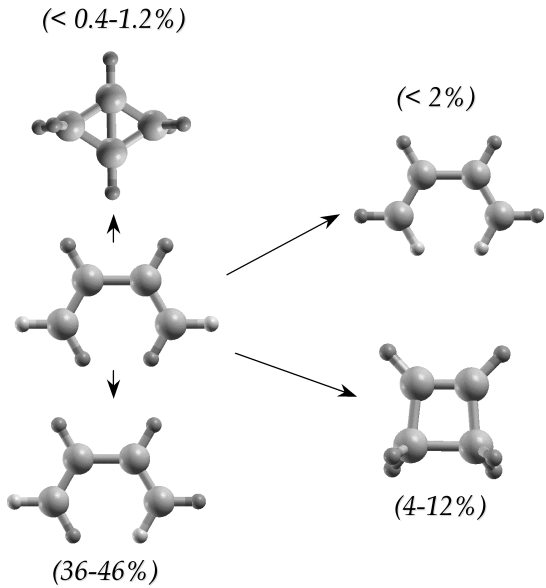

Fig. 7. Photoproduct distribution following irradiation of cis butadiene.

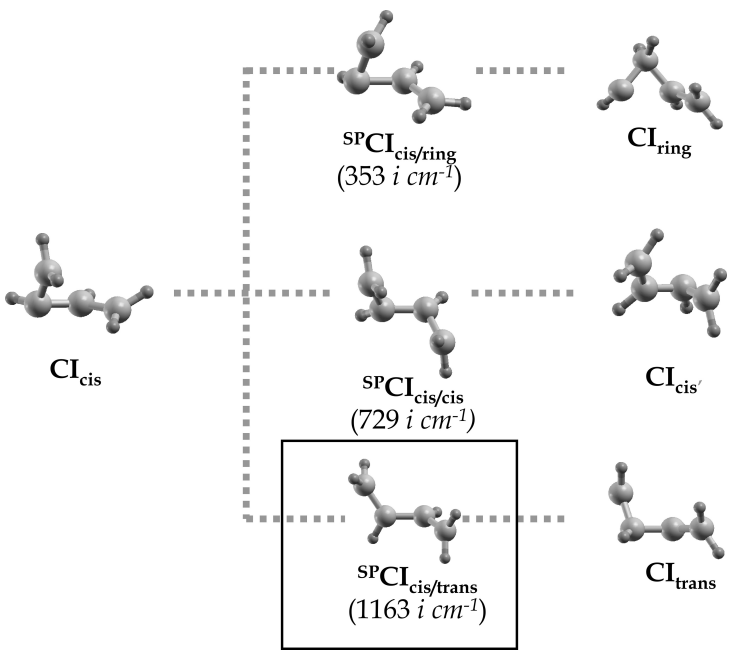

Fig. 8. Schematic representation of some minima and transition states on the extended seam for the S_1/S_0 intersection of butadiene.

4. Applications of the Extended Seam of a Conical Intersection to Photochemical Mechanisms

The extended seam concept is a mechanistic feature of many problems in photochemistry and photophysics, including photochromic systems such as dihydroazulene,[24] the ring opening of cyclohexadiene,[25,26] diarylethylenes,[27] protonated Schiff base rhodopsin models,[28] T-(ICT) compounds,[29,30] cyanine dyes,[31] biological chromophores such as PYP[32] and GFP,[33] excited state proton transfer,[34] the photochemistry of benzene,[14] the DNA bases,[35] and other organic transformations,[36–38] as well as classical problems in photophysics such as the photodissociation of formaldehyde.[39] In this section, we will choose a few examples (mainly from our own work) that illustrate the utility of the extended seam as a mechanistic feature in organic photochemistry.

4.1. *The photoinduced isomerization of 1,3-cyclohexadiene (CHD) to cZc-hexatriene (HT)*[25,26]

The ring opening of CHD is experimentally, as well as theoretically, a prototypical photochemical reaction involving an extended seam of conical intersections. In recent work,[40] we have been able to show (Fig. 9) that the seam is approximately parallel to the reaction path.

We have started with the discussion of this problem because, like fulvene, it is a "benchmark" of organic photochemistry. Nonadiabatic decay during a photochemical reaction was first clarified mechanistically by van der Lugt and Oosterhoff.[41] The central idea uses the concept of an avoided crossing (which provides the photochemical funnel) arising from the ground state and a doubly excited state along a common reaction coordinate (bond breaking, x axis in Fig. 9). However, the reaction path does not intersect with the conical intersection. Rather, as shown in Fig. 9, we have an extended seam lying approximately parallel to the excited state. This seam was computed via a seam MEP[13] (S_1-seam-MEP), which is similar to a conventional MEP but constrained to the intersection space. This motion orthogonal to the reaction path in the direction of the seam must control the ultrafast decay to the ground state.

In Fig. 9, we show the complete minimum energy S_0/S_1-CoIn seam (seam-MEP) for the conrotatory ring-opening reaction of CHD, covering the region from the closed (CHD) to the open ring structure (HT). The conrotatory S_1 IRC-MEP is almost parallel but displaced along a skeletal

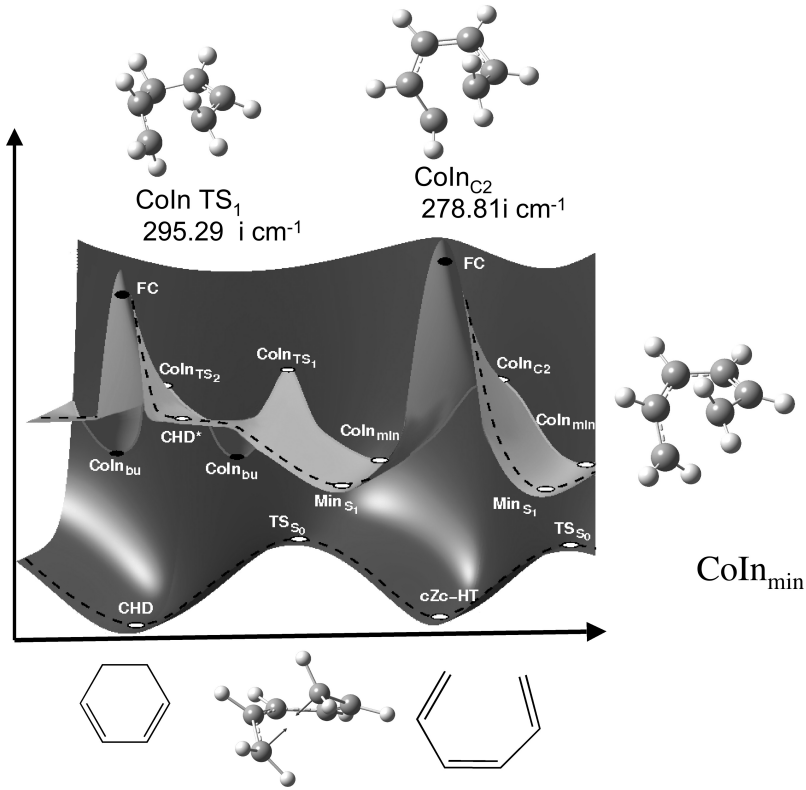

Fig. 9. Schematic representation of the S_0 and S_1 potential energy surfaces for the ring-opening/ring-closure reaction in the CHD/cZc-HT system including the conical intersection seam (seam-MEP). The reaction coordinate (RC) describes the conrotatory CHD-HT conversion along the minimum energy reaction path (IRC-MEP, dashed lines). The orthogonal BS vector is defined at every point along the seam-MEP as a linear combination of the branching space vectors critical points along the MEPs are noted with imaginary frequencies. (Adapted from Nenov *et al.*[40])

deformation coordinate. The avoided crossing feature (Min_{S_1}/TS_{S_0}) on the MEP is thus displaced from the lowest energy point of the conical intersection seam $\mathrm{CoIn}_{\mathrm{min}}$. Note that the seam-MEP has local transition state features (such as CoIn_{TS_1} and CoIn_{C_2}) and the corresponding imaginary frequencies are also given in Fig. 9. These frequencies were obtained using the second-order representation of the seam and correspond to motion along the intersection space (dominated by bond breaking). The seam

MEP can be mapped out in the intersection space as well, as discussed previously.[13]

In the Woodward–Hoffmann treatment of photochemistry as reformulated by van der Lugt,[41] the excited-state and ground-state reaction paths were assumed to be similar, with the "photochemical funnel" occurring at an avoided crossing. In this classic example, computations show that the ground, state and excited, state reaction paths are indeed very similar. However, CoIn seam is displaced from the excited-state/ground-state MEP along skeletal deformations, i.e. the branching space of the CoIn is orthogonal to the MEP.

4.2. *Diarylethylenes*[27]

These are remarkable photochromic systems where the chemical transformation is single bond breaking (Fig. 10). Because the distribution of π-bonds is different in both isomers, they have distinct absorption spectra. The photophysics and the efficiency of the system are completely controlled by the relationship between the reaction path and the degeneracy-lifting coordinates. From computations,[27] the similarity to the CHD example just discussed is remarkable.

Figure 11 shows the energy profile along a bond-breaking coordinate. We use labels CHD (cyclohexadiene) and HT (hexatriene) to emphasise the role of the central six carbon atoms and the relationship to the previous example. The crosses indicate points optimised on the conical intersection seam. Thus the "seam" does not appear to intersect with the reaction path. In Fig. 12, we show a 3D cartoon of the potential surface. In this figure, we also give the coordinates that lift the degeneracy (X_1 X_2) and the bond breaking reaction coordinate X_3. Like CHD and other examples we will discuss subsequently, the coordinates that lift the degeneracy are just skeletal deformations.

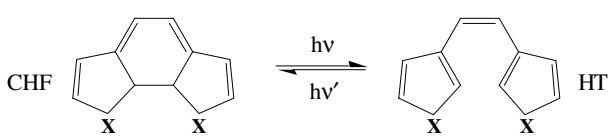

Fig. 10. Diarylethylenes with heterocyclic aryl and bisthienylethylene-based compounds (X = S) exhibit remarkable switching sensitivity (i.e. high quantum yield) and rapid response.

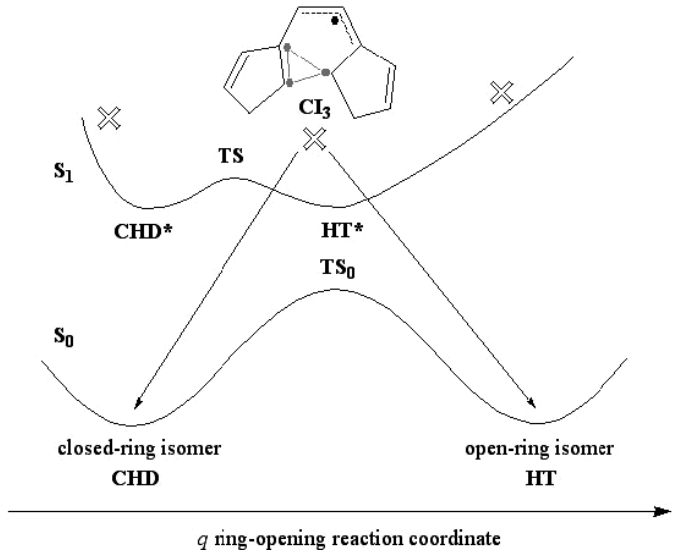

Fig. 11. Diarylethylenes: energy profile along the single bond breaking reaction path.

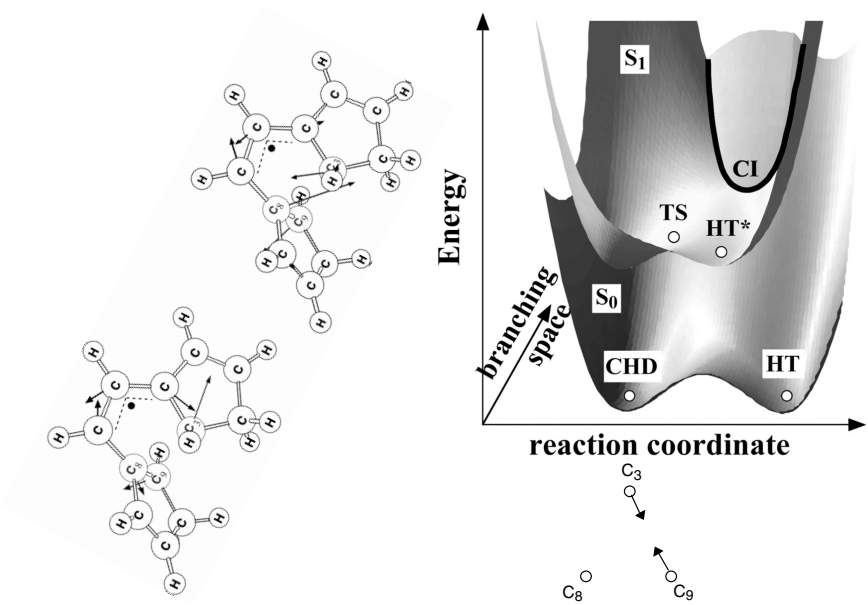

Fig. 12. A cartoon of the diarylethylene potential surfaces that can be distilled from the dynamics computations reported by Boggio–Pasqua *et al.*[27]

From Fig. 12 it is clear that there is a ground-state thermal reaction path involving a transition state $\mathbf{TS}_0$. In addition, there is an adiabatic reaction path on the excited state involving a minimum, a transition state **TS**, and another minimum. One can also find three critical points (local minima) on the conical intersection line indicated by crosses in Fig. 11: one near the products, one near the reactants, and also one near the transition state on the adiabatic excited-state reaction path. Thus, apparently disconnected conical intersections lie displaced along the intersection space coordinates (one of which is the transition vector shown in Fig. 12).

The conical intersection seam in Fig. 12 is very similar to CHD in Fig. 9: the reaction path is in the foreground (left to right), and the conical intersection line (**CI**) lies in the background. Thus the reaction coordinate is parallel to the seam and so decay to S_0 is controlled by motion orthogonal to the reaction path. The minimum energy point on the conical intersection line (middle cross, $\mathbf{CI}_3$ in Fig. 11) is the one that is located using gradient-driven optimization. While it appears quite close to the transition state on the excited state, it is actually on the HT side of the barrier.

In summary, we see that like CHD, knowledge of the excited-state reaction path does not yield an understanding of the photochromism of this system. Further, finding the conical intersection points does not yield a complete picture, because they do not lie on the reaction path. Indeed, a large segment of the intersection seam in this region is energetically accessible. However, to demonstrate and understand this, you need to run dynamics calculations.

Experimentally, one observes a fluorescence that is red-shifted, confirming that the position of the minimum is different on the excited state. The cyclization quantum yield (HT* to CHD) is high, which arises from the fact that a trajectory from **HT*** can sample the whole intersection seam, at right angles to the reaction path. On the other hand, for a trajectory starting from **CHD***, the probability of decay to S_0 is low, because the main locus of the conical intersection seam appears to be on the HT* side of the transition state. Thus to reach HT from CHD*, you have to pass through the transition state on the excited state reaction path. Thus there is a competition between passing through the transition state to reach the reactive conical intersection on the HT* side of the TS, and decay at a nearby crossing on the CHD* side of the transition state, which does not lead to any reaction. Thus the quantum yield is quite low in this direction.

There remains the question of whether one could design a pulsed laser sequence to "control" this reaction. For the HT isomer, one would want

a wavepacket with excess momentum in the branching space direction so that decay would take place quickly. In contrast, for the CHD isomer, one would need a wavepacket with excess momentum in the direction of the reaction coordinate, which would drive the reaction towards the transition state on the excited state and avoid competition with any nearby conical intersection points.

4.3. *The keto-enol tautomerism of o-hydroxyphenyl-(1,3,5)-triazine*

This species provides an efficient photostabilisation system.[34] This is an example where the extended conical intersection seam is one of the contributing factors controlling the efficiency in such species. The enol form [Fig. 13(a)] absorbs light and decays to the keto form [Fig. 13(b)] on the ground state. The ground-state keto form is metastable, and interconverts back to the enol form over a small barrier. Thus we have light absorption followed by no net chemical change and a photostabilising cycle. The low-lying excited states of such species are $\pi - \pi^*$, yet the hydrogen transfer involves the σ electrons. Thus the reaction coordinate X_3, since it involves these σ electrons, must be completely independent from the electronic state changes; the latter clearly involve only the π electrons. This is therefore an example where, *a priori*, the branching space coordinates must be completely different and independent from the reaction path, and one knows from the outset that the surfaces must involve the extended seam topology.

We begin with a VB analysis of ground and excited states at the enol and keto geometries. It is possible to classify the ground state and the two types of $\pi - \pi^*$ excited-state according to the number of π electrons

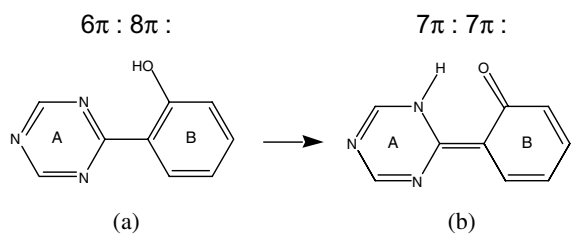

Fig. 13. Enol (a)–keto (b) tautomerism in o-hydroxyphenyl-(1,3,5)-triazine, indicating the number of π electrons in the ground state for each ring A and B. (Adapted from Paterson *et al.*[34])

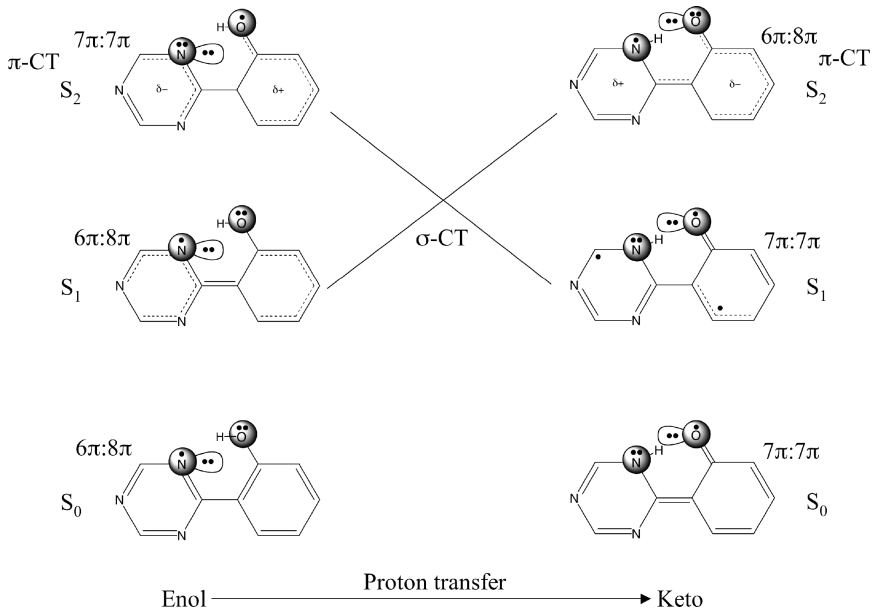

Fig. 14. Correlation diagram for the lowest $\pi - \pi^*$ excited states along a proton transfer coordinate. (Adapted from Paterson *et al.*[34])

associated with the two rings A and B (as indicated in Fig. 13). In Fig. 14, we show a valence bond correlation diagram for the lowest excited states along a proton transfer coordinate. This correlation diagram was elucidated by analysis of the excited states in recent theoretical calculations.[34] At a given geometry (keto or enol), the locally excited states preserve the number of π electrons in each ring, while the CT states change this population. (Notice that LE and CT, as we use them in this context, are relative to the ground state electronic configuration at a given geometry.) Thus, the state with the configuration $6\pi - 8\pi$ is locally excited at the enol geometry but formally CT at the keto geometry because of the migration of the proton. To avoid ambiguity, we will be classifying the excited states according to the number of π electrons in each ring. Only the ordering of the various states has to be determined from theoretical computations. However, it will be the vertical excitation to the CT state that will be observed experimentally, because of the larger oscillator strength.

If we look at the correlation (Fig. 14) between the enol ground state electronic configuration and the keto ground state configuration, we observe

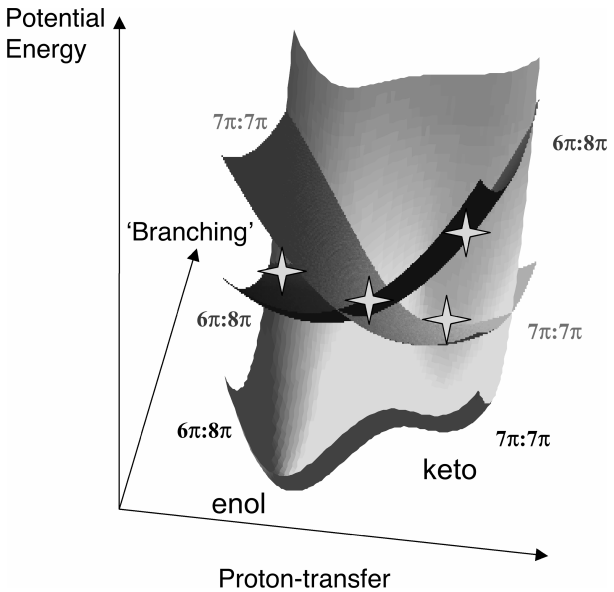

Fig. 15. A cartoon showing the lowest $\pi - \pi^*$ excited states along a proton transfer coordinate and a skeletal deformation coordinate from the branching space. (Adapted from Fig. 4 of Paterson *et al.*[34])

a change in the number of ring A and B electrons. One might expect an activation barrier due to the change in electronic configuration. In fact, computations[34] suggest that the barrier to back formation of the enol form from the keto form is small ($4\,\text{kcal mol}^{-1}$). Thus if the keto form is generated photochemically, the enol form will be rapidly regenerated thermally over a small barrier. It only remains to discuss the photochemical proton transfer to generate a ground state keto form.

The excited state proton transfer can be understood using Fig. 15, where we have labelled the various excited state potential energy surfaces consistent with Fig. 14. In Fig. 15, we show potential energy surfaces in a cartoon involving the proton transfer coordinate and one coordinate from the branching space of the extended conical intersection seam. We have optimized[34] four isolated critical points on the extended seam; three S_1/S_0 conical intersection points in the enol region, in the keto region and the transition state region as well as an S_2/S_1 conical intersection on the keto side as indicated by the four points/stars in Fig. 15. In each case, the branching space coordinates X_1 X_2 involve the skeletal deformations of the

two rings and do not include a component along the proton transfer coordinate. Thus in this case, the branching space is rigorously distinct from the reaction coordinate corresponding to proton transfer. Of course, along an adiabatic reaction path from the enol S_1 $6\pi - 8\pi$ minimum to the keto S_1 $7\pi - 7\pi$ minimum, the real crossing will become avoided and generates a transition state.

However, the initial excitation is to the enol S_2 $7\pi - 7\pi$ state. It is clear from Fig. 15 that there is an extended conical intersection seam between the $7\pi - 7\pi$ state/$6\pi - 8\pi$ excited states and the ground state. Thus the system can decay efficiently after photoexcitation at any point along the seam. Since the ground state barrier between the keto and enol form is negligible, the regeneration of the ground state enol form, following photoexcitation, must be exceedingly efficient. Thus the presence of a conical intersection seam along the reaction path, where the branching space coordinates are rigorously orthogonal to the reaction path, can be identified as a desirable design feature for efficient photostabilisers.

In summary, the extended seam of conical intersection, which is parallel to the reaction path, allows for radiationless decay at any point along the proton transfer reaction path, even on the enol side. This topology explains the experimental observation that the proton transfer is in competition with a temperature-dependent deactivation process. For photostability, this paradigm is ideal, since the seam has everywhere a sloped topology (gradients of ground and excited state are approximately parallel) and the ground state enol form is regenerated on an ultrafast timescale. These mechanistic features are independent of the ordering of the locally excited versus charge-transfer configurations. The notion of a seam of intersection explains the high photostability of the o-hydroxyphenyl-triazine class of photostabilisers in particular, but more generally highlights an important photochemical feature that should be considered when designing a photostabiliser.

In recent computations, we have been able to show that this same mechanism operates in other photostabilsers[42] and in a Watson–Crick base pair in DNA.[43] The reader is referred to Chap. 2 for further discussion.

5. Valence Bond Analysis of Conical Intersections

In this section, we would like to consider an example which illustrates how one can understand the occurrence of conical intersections, as well as the directions X_1 X_2 corresponding to the branching space, if one has an

understanding of the electronic (VB) structure of the two states involved. We address the following three questions:

(1) What is the connection between the molecular geometry and the electronic (VB) structure?
(2) Can the nature of the adiabatic and nonadiabatic pathways (and the position of the conical intersection) be predicted from VB structures?
(3) What is the VB origin of phase change when one does a circuit of a conical intersection?

5.1. *Twisted intermolecular charge transfer (T-(ICT)) in aminobenzonitrile (ABN) compounds*[29,30]

We will illustrate the first two points above using a T-(ICT) (twisted intermolecular charge transfer) aminobenzonitrile (ABN) compound (Fig. 16) as an example. We have recently completed theoretical work[29] on this

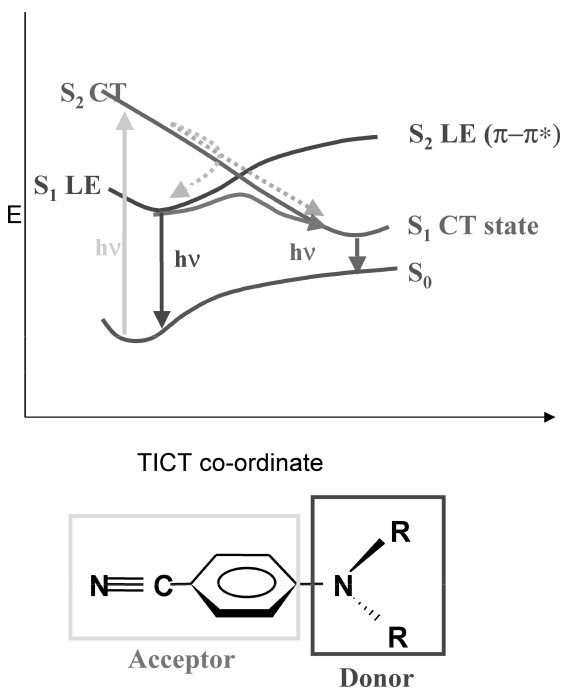

Fig. 16. Schematic representation of the T-(ICT) process and the emission of LE and ICT states.

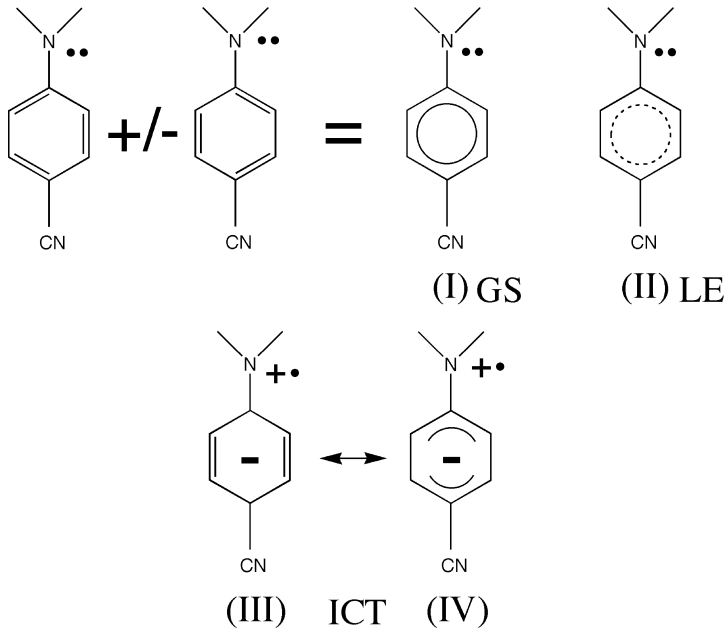

Fig. 17. VB states involved in the ICT LE surface in the T-(ICT) process. (Adapted from Gomez *et al.*[29])

class of compound and the reader is referred to that work for a complete bibliography.

In ABNs there are two low-lying excited states: a locally excited (LE) state where the excitation is localised on the phenyl ring (the ground state is the sum of the Rumer states while the LE state is the antiaromatic difference state), and the intramolecular charge transfer (ICT) state, where there is a transfer of charge from the amino group to the benzene ring (see Fig. 17). The ICT state is thus similar (electronically) to a benzene radical anion. In spectroscopy, with suitable substitution R and in the appropriate solvent, one can see emission from each state (LE or ICT diabatically, but both on S_1, see Fig. 16). The lowest energy equilibrium geometry of the ICT state is usually assumed to be twisted; hence the acronym T-(ICT). Since one observes dual fluorescence, there must be two S_1 minima, associated with the LE and ICT electronic structures (see Fig. 16). An adiabatic reaction path must therefore connect these two electronic structures on S_1. Thus there is an adiabatic reaction coordinate associated with the electron transfer process. However, the absorption from the ground state to

the LE state in the Franck–Condon region will be forbidden. Rather the absorption takes place to S_2, which is the ICT state at the Franck–Condon geometry. Thus there is also a nonadiabatic ICT process associated with the radiationless decay from S_2 (ICT) to S_1 (LE).

The ideas just discussed can be summarised in the potential energy diagram shown in Fig. 16. From the figure it is clear that the (adiabatic) state label S_1 and S_2 and the (diabatic) VB structure label ICT or LE are independent. The adiabatic reaction path involving a transition state (i.e. avoided crossing) appears to be associated with the real crossing. The T-(ICT) coordinate (amino group torsion) is assumed to be the reaction path. The transition state on this reaction path is associated with a state change from LE to ICT. This state change can also be associated with the nonadiabatic process via the real crossing. However, the real crossing and the nature of the branching space and its relationship to the adiabatic reaction path can only be understood by moving to higher dimensions and by consideration of the relationship between the branching space coordinates and the twisting coordinate.

We now give some discussion of the VB states involved in Fig. 16. In the ABN problem, there are four VB structures that are relevant and these are shown in Fig. 17. There are two "dot-dot" (covalent) configurations I and II and two zwitterionic configurations III and IV. Structures I and II are just the Kekulé and anti-Kekulé structures of benzene. The LE structure corresponds to the anti-Kekulé electronic structure, where excitation takes place in the phenyl ring. The zwitterionic structures III and IV are the ICT states. The ICT state has a positive charge on the amino group and an extra electron on the phenyl group and we expect similarities to the benzene radical anion. Thus there will be a quinoid (III) and an anti-quinoid structure (IV). In a theoretical calculation on ABN species, an inspection of the wavefunction will yield the information about which resonance structure dominates.

We are now in a position to discuss the reaction profile outlined in Fig. 16 in the full space of coordinates corresponding to the branching space X_1 X_2 of a conical intersection and the torsional coordinate X_3. This discussion will be focused on four related concepts:

(a) the S_2 to S_1 radiationless decay,
(b) the geometry and electronic structure of the two S_1 minima,
(c) the geometry of the S_1/S_2 conical intersection together with the nature of the X_1 X_2 branching space, and

(d) the nature of reaction path X_3 connecting the LE and ICT regions of S_1. Our objective is to rationalise all the data using the four VB structures in Fig. 17 and to illustrate the overall surface topology according to the models or cartoons given in Figs. 1 and 3.

In Fig. 18(a), we show the geometry of the S_2S_1 ICT/LE crossing (minimum energy crossing point), together with the directions $X_1$and X_2. The crossing occurs between the LE and ICT (III quinoid in Fig. 17) VB structures. The most important point about the geometry is that the amino group is not twisted. The directions X_1 and X_2 are mainly the skeletal deformations of the phenyl ring and do not involve torsion. This is completely consistent with the fact that the LE and ICT VB structures differ essentially only in the phenyl ring. Thus we have established that the nonadiabatic decay does not involve the amino group twist, since the directions X_1 and X_2 exclude this coordinate. This in turn follows from the bonding pattern of the two VB states.

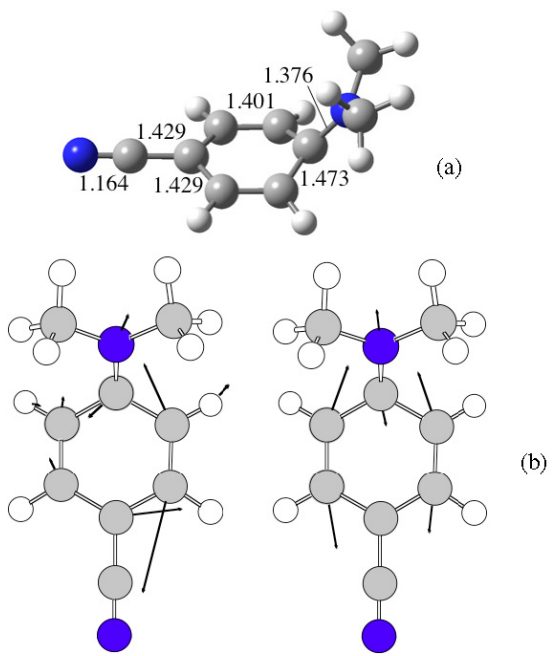

Fig. 18. (a) Geometry of the S_2S_1 ICT/LE crossing MECI, together with (b) the directions X_1 and X_2 for ABN systems. (Adapted from Gomez *et al.*[29])

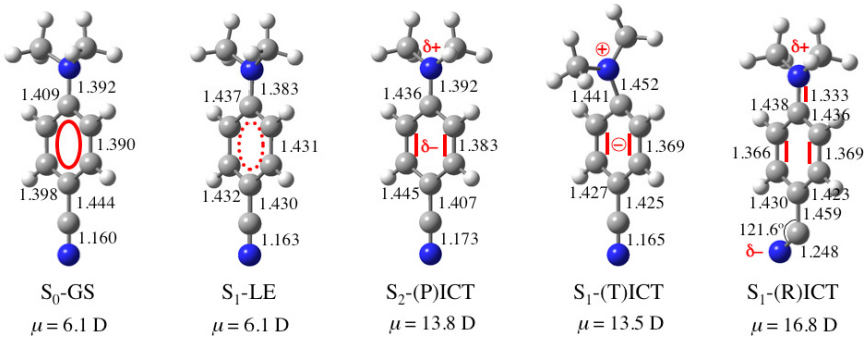

Fig. 19. The geometries of various minima on the ABN S_2 and S_1 states. (Adapted from Gomez *et al.*[29])

Let us now consider the geometries of the various minima on the S_2 and S_1 states shown in Fig. 19. Notice that we are careful to include both the adiabatic label S_2 S_1 and the diabatic VB state label LE or ICT. One can see that the main difference in the "dot-dot" covalent VB structures associated with S_0-GS and S_1-LE geometries occurs in the C-C bond lengths of the phenyl ring, which are lengthened in S_1-LE because of the anti-Kekulé nature of the VB structure. If we examine the CT structures, we see that we have a planar (P)-ICT structure on S_2 and a twisted (T)-ICT structure on S_1. (There is also a high-energy (R)-ICT structure that has a bent cyano group.) The reaction pathways that connect these structures must include (i) an adiabatic reaction path that connects the S_1-LE and (T)-ICT structures on S_1 along a torsional coordinate and (ii) a nonadiabatic reaction path that connects the S_2 planar (P)-ICT structure with the S_1-LE structure and the S_1 (T)-ICT structure via an extended conical intersection seam, that lies along a torsional coordinate. We now discuss this.

The optimised geometries of the various minima on S_2 and S_1 (Fig. 19), together with the nature of the branching space vectors X_1 X_2 [Fig. 18(b)], suggests that the topology of the potential surface has the form shown in the model surface in Fig. 3. Thus we have a conical intersection seam along $X_3 = NR_2$ torsion with the branching space X_1 X_2 spanning the phenyl group skeletal deformations shown in Fig. 18(b). We collect together all of the information in Fig. 20, corresponding to the general model given in Fig. 3. At the left-hand side, corresponding to untwisted geometries, one can see the S_1-LE minimum and the planar S_2(P)-ICT state minima. Because the branching space excludes $X_3 = NR_2$ torsion, the conical intersection seam

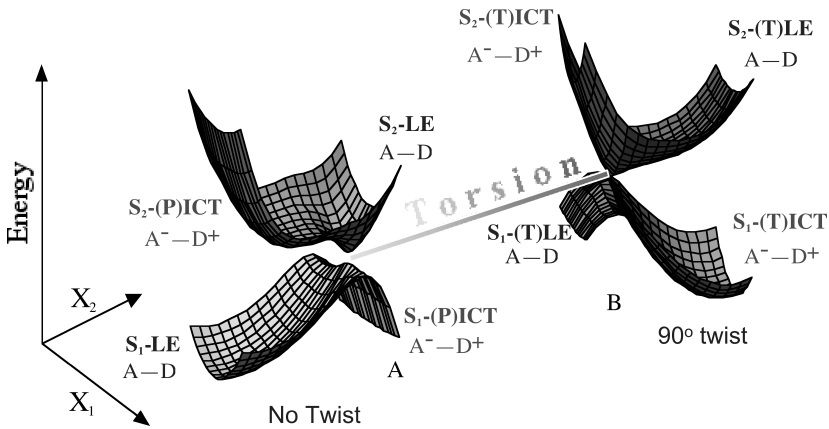

Fig. 20. The geometries from Fig. 19 located in the cone that changes shape along the conical intersection hyperline. (Adapted from Gomez *et al.*[29])

can persist as an extended seam along this coordinate. The double cone at the twisted geometry is shown on the right-hand side of the figure. Here the double cone shape changes and the twisted S_1(T)-ICT state minima develops. Thus we have added the two branching space dimensions X_1 X_2 to Fig. 16 to yield Fig. 20. The origin of the nonadiabatic S_2 to S_1 process is now clear. The initially created state at the Franck–Condon geometry is near the S_2(P)-ICT state minimum. This state can decay to either the S_1-LE minimum or the S_1(T)-ICT minima along the extended seam. The S_1 adiabatic process can occur following S_2(P)-ICT to S_1-LE decay via a path on S_1 involving the $X_3 = NR_2$ torsion.

5.2. *What happens when one does a conical intersection circuit in the branching plane?*[44–47]

The 1975 paper of Longuet–Higgins[48] states the phase change theorem as:

> *"If the wavefunction of a given electronic state changes sign when transported round a loop in nuclear configuration space, then the state must become degenerate with another one at some point within the loop."*

This theorem has implications for dynamics[49] and can even provide a method for optimising a geometry.[46] However, it is more interesting when applied using the VB method to understand the chemical nature of the conical intersection. Haas and his co-workers have developed this idea[44] and Vanni *et al.*[45] have attempted to make these ideas more rigorous. Many

years ago, we attempted to rationalise the geometries of conical intersections of hydrocarbons using VB theory.[50,51] It turns out that the phase change rule, when applied to three and four electrons, gives additional insights into the chemical nature of conical intersections. We now give a discussion adapted from the work of Vanni *et al.*[45]

It turns out that for the case of three orbitals and three electrons or four orbitals and four electrons, where the orbitals are 1s orbitals, one has some simple analytical results that enable one to understand the branching space coordinates and the relationship to valence bond structures. Of course the results are rigorous only in these cases, but they can be applied in a qualitative way to other examples.

Valence bond theory uses a special combination of determinants called Rumer functions. For three orbitals and three electrons, one has three valence bond structures as shown in Fig. 21. The valence bond structures such as A can be defined in terms of determinants as

$$A = \frac{1}{\sqrt{2}}\{|\,1 \quad \bar{2} \quad 3\,| - |\,\bar{1} \quad 2 \quad 3\,|\}, \tag{12}$$

where we use $||$ to denote the diagonal elements of the determinant. However, it is simpler to formulate arguments directly in the Rumer basis.

In this three-electron example, if the ground state wavefunction is A, then the corresponding excited state wavefunction would be B (since there are only two linearly independent spin functions). There are two complications in practice. Firstly, A and B are not orthogonal if we use Rumer VB functions. The overlap between the Rumer functions A and B is $\langle A|B\rangle = -\frac{1}{2}$. Thus, if we take A to be a ground state wavefunction, the corresponding orthogonal excited state wavefunction B must be Schmidt orthogonalised to give $B'' = \frac{2}{\sqrt{3}}\big(B + \frac{1}{2}A\big)$. Secondly, the valence bond structure C is not linearly independent of the other two structures. Thus we have $C = A + B$ and C is linearly dependent on A and B. The excited state partner functions constructed in this way, which correspond to the

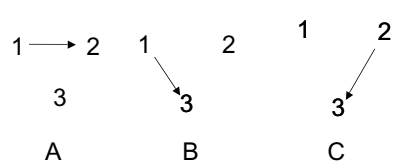

Fig. 21. Rumer VB diagrams for a three orbital three electron system.

VB functions A and B in Fig. 21, are shown in Eq. (13a) below:

$$A'' = \frac{2}{\sqrt{3}}\left(A + \frac{1}{2}B\right),$$
$$B'' = \frac{2}{\sqrt{3}}\left(B + \frac{1}{2}A\right). \tag{13a}$$

Similarly, the orthogonal partner function (C'') of C can be taken as

$$C'' = \frac{1}{\sqrt{3}}(A - B), \tag{13b}$$

where the $\sqrt{3}$ in C'' comes from the normalisation requirement since A and B are not orthogonal. (Observe the notation: C'' is the excited state orthogonal state to C itself, while A'' is the orthogonal state of A obtained by Schmidt orthogonalising A to B, and B'' is the orthogonal state of B.)

Now let us define the branching plane, X_1 X_2. We can make any choice of orthogonal states as a starting point, but we shall choose the states $C = A + B$ and $C'' = \frac{1}{\sqrt{3}}(A - B)$ to simplify the algebra.

However, first we must establish an approximate but essential relationship between nuclear configurations and VB structures. The matrix elements between Rumer functions involve exchange integrals K_{ij}($K_{ij} = [ij|ij] + S_{ij}h_{ij}$ in the case of 2 H atom 1s orbitals). The indices ij are associated with orbitals on nuclear centres i and j. Thus in Fig. 21, the indices 1, 2 and 3 relate to nuclear centres 1, 2 and 3. Thus our discussions are rigorous only for 3 H atoms with a single 1s function on each centre. However, the relationships would be expected to hold approximately for any set of three nuclei with one "active" VB orbital on each centre.

As stated above, for our computation of the branching space, we use the ground $C = A + B$ and excited $C'' = \frac{1}{\sqrt{3}}(A - B)$ orthogonal states. The branching space directions require the computation of the direction of the derivatives of energy difference $\Delta H(H_{CC} - H_{C''C''})$ and off-diagonal matrix element $H_{CC''}$. The AB, BC matrix elements of the Hamiltonian are between the Rumer basis states.[45] A, B and C are collected in Eq. (14).

$$H_{AA} = K_{12} - \frac{1}{2}(K_{13} + K_{23}),$$
$$H_{BB} = K_{13} - \frac{1}{2}(K_{12} + K_{23}),$$
$$H_{CC} = K_{23} - \frac{1}{2}(K_{12} + K_{13}),$$

$$H_{AB} = \frac{1}{2}(K_{12} + K_{13} - 2K_{23}),$$
$$H_{AC} = -\frac{1}{2}(K_{12} + K_{23} - 2K_{13}),$$
$$H_{BC} = \frac{1}{2}(K_{13} + K_{23} - 2K_{12}). \tag{14}$$

All other matrix elements can be derived from these equations. The energy difference is[45]:

$$(X_1):$$
$$\Delta H = H_{C,C} - H_{C''C''} \tag{15}$$
$$= -\frac{5}{3}(K_{12} + K_{13} - 2K_{23}),$$

and the interstate coupling is[45]

$$(X_2):$$
$$H_{C,C''}(q) = \frac{1}{\sqrt{3}}\langle A - B|H|A + B\rangle \tag{16}$$
$$= \frac{\sqrt{3}}{2}(K_{13} - K_{12}).$$

The derivatives can then be expressed qualitatively as follows. The indices ij in the exchange integrals K_{ij} relate to orbitals on centres i and j and $K_{ij} \propto \exp(-bR_{ij})$ where R_{ij} is the distance between centres i and j. Thus the magnitude of the gradient is $dK_{ij}/dR_{ij} \propto \exp(-bR_{ij})$ with direction along a unit vector from centre i to centre j. For this reason we can use the direction of ΔH and $\nabla(\Delta H)$ interchangeably and similarly for H_{AB}.

We now illustrate this idea. For each exchange integral $-K_{ij}$, we draw a vector on atom i heading towards atom j and a vector on atom j heading towards atom i (for K_{ij} two vectors are the opposite of the ones above). We then compute a resultant vector for each atom of the system. The "resultant" will qualitatively describe the gradient difference vectors. For the three-orbital example, we have the result shown in Fig. 22.

For $H_{CC''}(K_{13} - K_{12})$ coordinate we have the following: on atom 1 the resultant vector is the sum between two vectors arising from two terms: $-K_{12}$ and K_{13}, while on atom 2 the resultant vector arises only from $-K_{12}$, and on atom 3 the resultant vector arises only from K_{13}. For the $H_{CC} - H_{C''C''}$ coordinate $(K_{12} + K_{13} - 2K_{23})$ we have the following: on atom

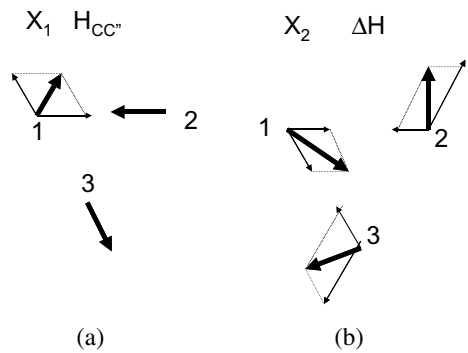

Fig. 22. Derivative coupling and gradient difference associated with ΔH and $H_{CC''}$ coordinates for three orbital three electron systems. Note that we use ΔH and its gradient interchangeably because they are parallel as discussed in the text. (Adapted from Vanni *et al.*[45])

1 the resultant vector is the sum between two vectors arising from two terms: $-K_{12}$ and $-K_{13}$; on atom 2 the resultant vector is the sum between two vectors arising from two terms: $-K_{12}$ and $2K_{23}$; and on atom 3 the resultant vector is the sum between two vectors arising from two terms: $-K_{13}$ and $2K_{23}$. Thus the $\delta\kappa \equiv \left.\frac{\partial(E_B - E_A)}{\partial Q_{x_1}}\right|_0$ and $\kappa^{AB} \equiv \left.\frac{\partial\langle\Psi_A|\hat{H}|\Psi_B\rangle}{\partial Q_{x_2}}\right|_0$ corresponding to the $H_{CC} - H_{C''C''}$ and $H_{CC''}$ derivatives are shown as the axes in Fig. 22. We can see that the condition $H_{CC} - H_{C''C''} = 0$ is achieved when $K_{12} + K_{13} = 2K_{23}$. Along the $-\mathrm{H}_{CC''}$ coordinate at the origin, $K_{13} = K_{12}$. Thus at the apex of the cone, one has

$$K_{12} = K_{13} = K_{23} \tag{17}$$

corresponding to an equilateral triangle, a well-known result.[50]

Now we would like to explore the relationship between molecular structure and VB (i.e. electronic structure) illustrated in Fig. 23. Figure 23 shows the branching space directions (see Fig. 22) as deformations of the three atoms together with three molecular structures where the VB structure (i.e. the electronic structure) is coincident with the nuclear geometry. Notice that they are related by a rotation (ϕ) in the plane of 120° in the space of nuclear coordinates. It is easily demonstrated that the valence bond wavefunctions are obtained by rotation (θ) of ground and excited state of VB structures by 60°. Thus there is a fundamental relationship between electronic structure and nuclear structure in the vicinity of a conical intersection with a special case of three electrons in three hydrogen like 1s orbitals. (The

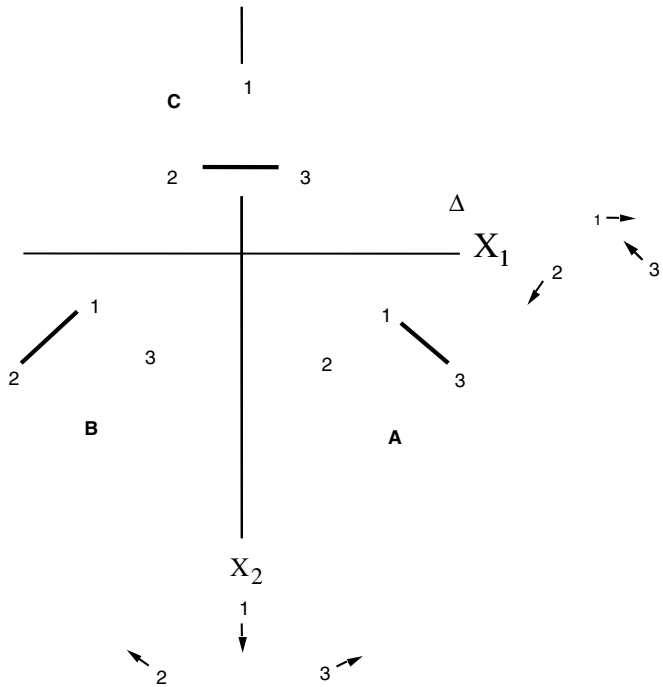

Fig. 23. The ϕ loop in nuclear configuration space showing Valence Bond structures for the three orbital three electron problem and the ΔH and $H_{CC''}$ vectors which define the branching plane. (Adapted from Vanni *et al.*[45])

same results can be obtained for four orbitals and four electrons.) There is thus a relationship between the polar angle in a closed loop around the apex of the cone (ϕ) (relating the molecular structures) and the mixing angle (θ) (relating the VB structures) of the ground and excited state $\begin{bmatrix} \Psi_A \\ \Psi_B \end{bmatrix}$ wavefunctions under the transformation T.

We now expand on this observation. We define a 2×2 transformation T as

$$\mathbf{T}(\mathbf{q}) = \begin{bmatrix} \cos\theta(\mathbf{q}) & -\sin\theta(\mathbf{q}) \\ \sin\theta(\mathbf{q}) & \cos\theta(\mathbf{q}) \end{bmatrix}. \tag{18}$$

The angle θ depends on the polar angle ϕ only. It is therefore constant along straight lines having their origin at the apex of the double cone. Matrix rotations θ by 60° and 120° [Eq. (19) below] corresponding to the

geometry changesϕ of 120° and 240° involve application of the transformations in Eq. (19) to C and C″

$$\begin{bmatrix} \frac{1}{2} & -\frac{\sqrt{3}}{2} \\ \frac{\sqrt{3}}{2} & \frac{1}{2} \end{bmatrix}, \quad \begin{bmatrix} -\frac{1}{2} & \frac{\sqrt{3}}{2} \\ -\frac{\sqrt{3}}{2} & -\frac{1}{2} \end{bmatrix}, \tag{19}$$

It is easily shown that for a 60° rotation we have

$$\begin{bmatrix} C = A + B \\ C'' = \frac{1}{\sqrt{3}}(A - B) \end{bmatrix} \Longrightarrow \begin{bmatrix} B \\ A'' = \frac{2}{\sqrt{3}}\left(A + \frac{1}{2}B\right) \end{bmatrix}. \tag{20}$$

The whole loop in θ is shown in Fig. 24 (without normalization factors). Thus we have a correspondence between molecular structure and VB structure as we do a circuit around a conical intersection.

It is also instructive to examine a special case. Consider the loop of radius $\rho = a$ passing through $(\phi = 0)\,(a_{x_1}, 0)$; $(\phi = \pi)(-a_{x_1}, 0)$; $(\phi = 2\pi)$ $(a_{x_1}, 0)$. The corresponding rotation matrices are

$$\begin{bmatrix} 1 & 0 \\ 0 & 1 \end{bmatrix}, \quad \begin{bmatrix} 0 & -1 \\ 1 & 0 \end{bmatrix}, \quad \begin{bmatrix} -1 & 0 \\ 0 & -1 \end{bmatrix}. \tag{21}$$

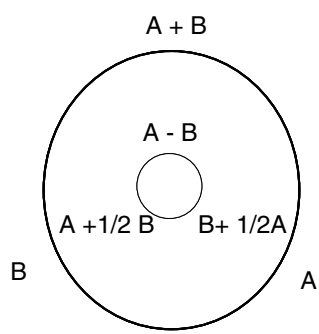

Fig. 24. Loop θ in valence bond structure space for the three orbital three electron problem. The outer loop corresponds to the ground state VB structures while the inner loop corresponds to the excited state VB structures that have been Schmidt orthogonalised but not normalised. (Adapted from Vanni *et al.*[45])

Thus looking at the first row, states X and Y transform according to Eq. (22) to give

$$\begin{aligned} X &\to \frac{1}{\sqrt{2}}(X-Y) \to -Y \to -\frac{1}{\sqrt{2}}(Y+X) \to -X, \\ Y &\to \frac{1}{\sqrt{2}}(Y-X) \to -X \to -\frac{1}{\sqrt{2}}(X+Y) \to -Y. \end{aligned} \tag{22}$$

There are two important observations: (1) X and Y are interchanged on rotation through 90° and (2) we have a phase change as one rotates a full circle.

Now let us look at an application. The theory we have just developed holds rigorously only for three electrons in three 1s orbitals. However, the principles based upon overlap remained approximately valid. This is illustrated in Fig. 25 where we show a circuit of the prefulvene-like conical intersection in benzene.[52] Our purpose here is to illustrate the circuit of the conical intersection that we have described in the preceding discussion. In Fig. 25 the three valence bond structures A, B and C that lie on the circuit correspond to the couplings of the carbon atoms involved in the "prow" of the prefulvene conical intersection. Notice that the 180° rotation in the geometrical plane exchanges an excited state valence bond structure

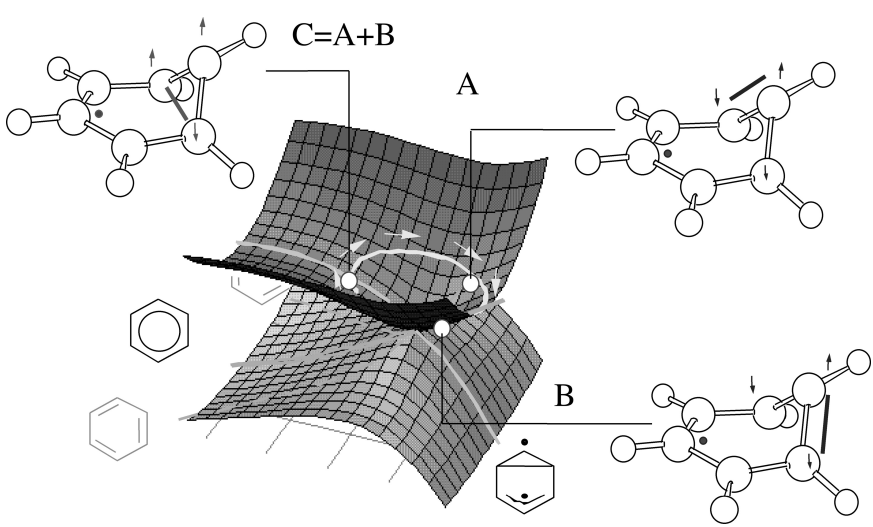

Fig. 25. A circuit of the prefulvene-like conical intersection in benzene.[52] (Adapted from Robb *et al.*[67])

so that we see the image of structure C on the ground state. Thus for the benzene conical intersection, the circuit about the apex of the cone (Fig. 25) traces out the valence bond structures corresponding to Figs. 21 and 23.

The same type of manipulations can be carried out for four orbitals and four electrons in the same fashion.[45] Unfortunately, for systems larger than four orbitals one cannot do the manipulations analytically. Nevertheless, if one can identify the valence bond structures for ground and excited state at one point on the circuit, then one can still apply the transformation of Eq. (8) to generate remaining valence bond structures that lie on the circuit.

Haas and co-workers have looked at many examples.[44,46,53] In applying such methods qualitatively, one needs to be clear that (a) the circuit of the conical intersection must be in the branching plane and (b) the phase change involves a wavefunction where the VB components involve two linearly independent VB functions corresponding to ground and excited state at one reference point. In the case of six orbitals and six electrons, there are five independent singlet spin functions. In order to apply the phase change method correctly, one needs to choose two linearly independent combinations. As we have shown[45] elsewhere, this is not trivial. Thus the method is probably more useful for three and four electron systems where it can be easily applied qualitatively.

6. Exploring the Conical Intersection Seam using Dynamics

Dynamics methods are becoming essential for the study of nonadiabatic events.[6,54] This subject will be treated by several contributors to this book, so we will limit ourselves to some studies that show how dynamics can sample the extended conical intersection seam and provide mechanistic information that would not be available from reaction path studies.

6.1. *A model cyanine system: The extended seam for cis-trans double bond isomerization*[31,55]

We now turn to the cyanine dye 1,1′-diethyl-4,4′-cyanine (1144-C) shown in Fig. 26(a). Experiments demonstrate[56] that one may control the cis-trans isomerisation by populating vibrational modes orthogonal to an extended seam of intersection. We have[31,55] mapped the potential surface for the model shown in Fig. 26(b).

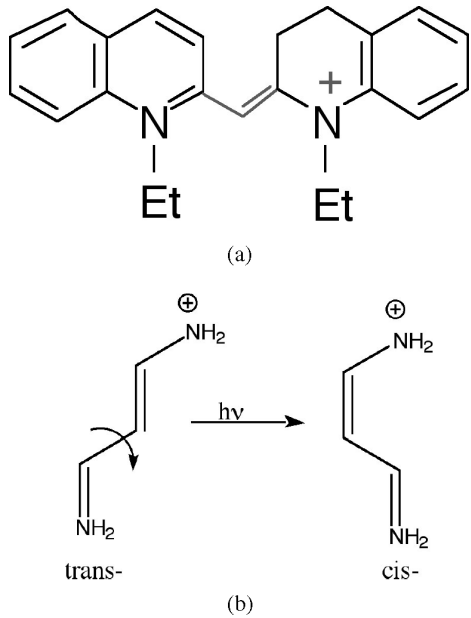

Fig. 26. (a) Cyanine dye 1,1′-diethyl-4,4′-cyanine (1144-C). (b) Three-carbon model of 1144-C.

The reaction coordinate X_3 (Fig. 2) is cis-trans isomerisation. The branching space is symmetric and anti-symmetric skeletal deformation coupled with pyramidal NH_2 distortion. Thus the seam is accessible along the skeletal deformation coordinate before cis-trans isomerisation can occur. Our dynamics results[31] (classical trajectories with a surface hop where the gradient comes from CASSCF) are summarised in Fig. 27. Figure 27 shows the geometries where the system hops. The minimum on the seam occurs at a dihedral angle of around 104°. However, most of the trajectories hop before the molecule has completed the half-rotation. Thus dynamics computations suggest that for the cyanine dye example, the sand flowing through the funnel (decay at the minimum of the conical intersection seam) (Fig. 1) is not applicable and the system samples the seam at all torsion angles (Fig. 2).[a]

[a]Since writing this review we have completed quantum dynamics computations [C.S. Allan, B. Lasorne, G.A. Worth and M.A. Robb, A straightforward method of analysis for direct quantum dynamics: application to the photochemistry of a model cyanine, *J. Phys. Chem. A,* **114**(33), 8713–29 (2010)]. The results are qualitatively similar.

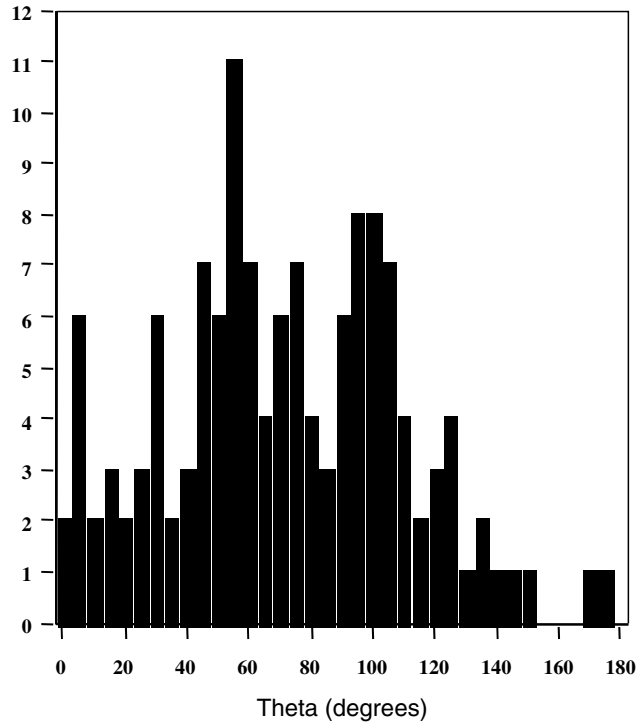

Fig. 27. Surface hop angle along cis-trans isomerisation coordinate for three-carbon model of 1144-C.[31]

6.2. *Benzene*

The photochemistry and photophysics of Benzene is another "benchmark" problem in organic photochemistry.[57,58] Recently,[14,59] dynamics computations have been carried out on this system using variational multiconfiguration Gaussian wavepackets.[60] The cartoon shown in Fig. 28 shows the potential surface in the space of the prefulvene distortion that leads to the conical intersection (one of the branching space coordinates) and the ring-breathing mode (an intersection space coordinate). The extended seam develops along this coordinate. Remarkably, the conical intersection is peaked near the prefulvene-like minimum of the conical intersection but sloped further along the seam. This suggests that whether the system decays at the peaked geometry and produces a prefulvene-like product or decays at the sloped part of the seam, regenerating the reactant, might be controlled by the energy in the ring-breathing mode.

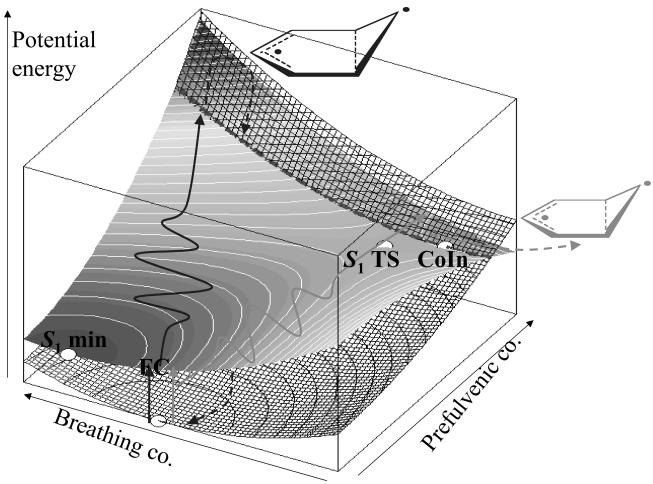

Fig. 28. Controlling the S_1 photochemistry of benzene: targeting the sloped part of the conical intersection leads to regeneration of benzene (photophysics); targeting the opposite end of the seam yields the benzvalene at a peaked conical intersection (photochemistry). (Adapted from Lasorne *et al.*[59])

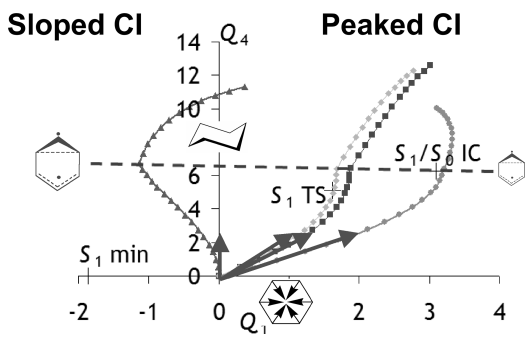

Fig. 29. Four quantum trajectories differing by the value of the initial momentum k_1 along coordinate Q_1 (projection in the (Q_1, Q_4)-subspace). Dashed line is the seam of intersection between diabatic states (prefulvenoid structures of various sizes, as indicated by molecular structures). (Adapted from Lasorne *et al.*[59])

The results are summarised in Fig. 29.[59] In this figure we show the propagation of the centre of the wavepacket for various initial conditions (arrows) involving the prefunvene (Q_4) and ring-expanding mode (Q_1). It is clear that the point of decay on the seam can indeed be controlled theoretically. Momentum in ring expansion (negative Q_1) leads to decay at the sloped intersection. Alternatively, ring contraction (positive Q_1) leads

to decay at prefulvene. Thus, like the cyanine example discussed previously, quantum dynamics[60] may suggest new experiments for controlling photochemistry.

6.3. *Biological chromophores: PYP*[32,61]

In biological chomophores, nature controls photochemistry via the structure of the protein in which the chromophore is embedded,[32,33,61−63] As the last example, we briefly discuss the cis-trans isomerisation of a double bond in the covalently bound *p*-coumaric acid chromophore (Fig. 30) in Photoactive Yellow Protein (PYP), an archetypal reversible protein photoreceptor.[32,61]

A combination of *ab initio* (CASSCF) dynamics with surface hopping and classical molecular dynamics (MD) simulation techniques has been used to directly simulate the process of photoisomerisation within the protein.[32,61] We have used CASSCF for the chromophore itself and

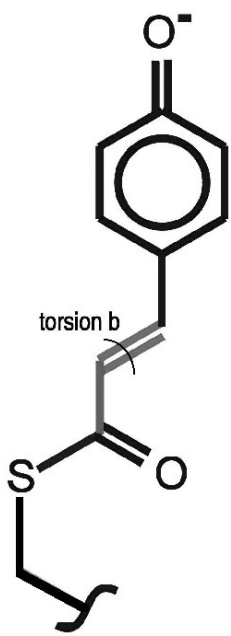

Fig. 30. The *p*-coumaric acid chromophore in PYP. The chromophore is covalently linked to the side chain of Cys69 through a thioester bond. The *p*-hydroxyphenyl moiety is deprotonated, but stabilised by hydrogen bonding interactions with the side chains of Tyr42 and Glu46. (Adapted from Groenhof *et al.*[32])

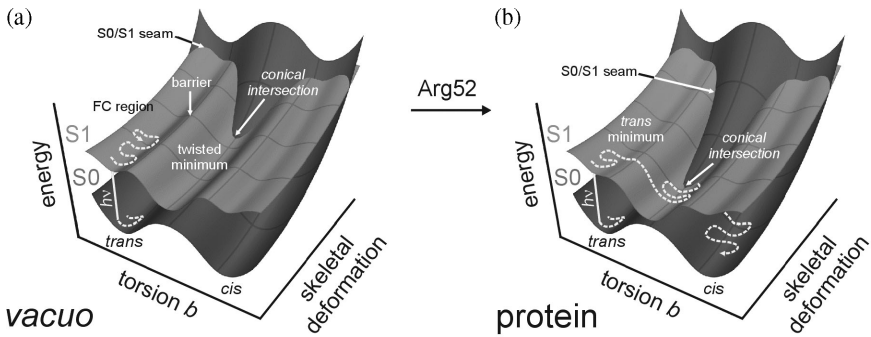

Fig. 31. Potential energy surfaces of the excited and ground states in the *trans*-to-*cis* isomerisation coordinate (torsion *b*, Fig. 30) and a skeletal deformation of the bonds: in *vacuo* (a) and in the protein (b). (Adapted from Groenhof *et al.*[32])

molecular mechanics for the remainder of the system. A cartoon of the potential energy surfaces in vacuo and in the protein is shown in Fig. 31.

The extended seam is present for both vacuo and protein along the cis-trans isomerisation coordinate. Again, the coordinates that lift the degeneracy are the skeletal deformations. In vacuo [Fig. 31(a)], there is an excited-state transition state with barrier and minimum where the chromophore is partly twisted, as well as a minimum with a half twist. In the protein [Fig. 31(b)], the S_1 surface is stabilised by the arg52 residue and the conical intersection seam is displaced so that it intersects with the reaction path. Thus the conical intersections in the protein and in the gas phase are significantly different. In the gas phase, substantial additional skeletal deformation motion to reach the seam would be required at the half twist geometry.

In the gas phase dynamics, using the same initial conditions as in the protein simulations, the system never makes it over the first partial twist torsion barrier. In contrast, in the protein, the excited state is specifically stabilised by the charge distribution of the protein (arg52). One observes a decrease of the S_1-S_0 energy gap in the region of the twisted intermediate (from 80 kJ mol^{-1} in vacuo to less than 1 kJ mol^{-1} in the protein), accompanied by a displacement of the crossing seam closer to the global minimum. One also sees a decrease of the energy barrier separating the early planar S_1 minimum and the twisted S_1 minimum. In total, 14 dynamics simulations are discussed in Ref. 32. In the protein, the lifetime of the excited state ranged from 129 to 2293 fs. The ratio of the number of successful isomerisations to the number of excited-state trajectories is ∼0.3, close

to the experimental quantum yield of 0.35. Statistically, the number of trajectories is small, but it nevertheless yields a consistent mechanistic picture.

PYP is probably the most dramatic example of a situation where the reaction path is simple (just torsion), and orthogonal to the degeneracy-lifting coordinates (mainly skeletal deformations). In this case, the reactivity is changed when you add the electric field of the protein. Nature has been very careful to position one charged residue in exactly the right place.

7. Conclusions

With developments in theory and computation (see subsequent chapters in this book), quantum dynamics computations[6,14,64] are becoming possible as a method to study nonradiative decay at conical intersections in organic photochemistry. Here a more direct interaction with time-resolved laser methods becomes possible, so that control of photochemistry becomes possible.[65] Recent results show that the extended seam is a common mechanistic feature and this may be useful for the control of photochemistry either by lasers or by chemical substitution. The other major challenge is applications to biological systems.[62,66] Again the extended seam appears to play a role. However, developments in theory are needed to allow for quantum effects in nuclear motion in combination with force field methods and to allow for multi-scale effects.

Acknowledgments

Some of the discussion of the mathematical character of the extended seam (Sec. 2.1) has been adapted from the PhD Thesis of Fabrizio Scilia (University of London, 2008). Our work on photochemistry was started in collaboration with Massimo Olivucci and the late Fernando Bernardi. Much of the work discussed in this article has involved many other senior collaborators (Luis Blancafort, Mike Bearpark and Graham Worth), recent postdocs (Martial Boggio-Pasqua, Benjamin Lasorne, Martin Paterson) who now hold tenured academic positions and recent PhD students (Fabrizio Scilia, Stefan Vanni). Articles such as this, which collect many ideas and thoughts, are only possible through the dedicated hard work of co-workers over many years that helped develop them.

References

1. F. Bernardi, S. De, M. Olivucci and M.A. Robb, *J. Am. Chem. Soc.* **112**(5), 1737 (1990).
2. M. Klessinger and J. Michl, *Excited States and Photochemistry of Organic Molecules* (1995).
3. N.J. Turro, V. Ramamurthy and J. Scaiano, *Modern Molecular Photochemistry of Organic Molecules* (2010).
4. A. Migani and M. Olivucci, in *Conical Intersections*, edited by W. Domke, D.R. Yarkony and H. Koppel p. 271 (2004).
5. M.J. Paterson, M.J. Bearpark, M.A. Robb, L. Blancafort and G.A. Worth, *Phys. Chem. Chem. Phys.* **7**(10), 2100 (2005).
6. G.A. Worth, M.A. Robb and B. Lasorne, *Mol. Phys.* **106**(16–18), 2077 (2008).
7. M.J. Bearpark and M.A. Robb, in *Reviews of Reactive Intermediate Chemistry*, edited by M.S. Platz and R.A. Maitland John Wiley & Sons, Inc, pp. 379 (2007); G.A. Worth, M.J. Bearpark and M.A. Robb, in *Computational Photochemistry* edited by M. Olivucci (Elsevier), pp. 171 (2005).
8. L. Blancafort, B. Lasorne, G.A. Worth and M.A. Robb, in *The Jahn-Teller-Effect Fundamentals and Implications for Physics and Chemistry* edited by H. Köppel, D.R. Yarkony and H. Barentzen (Springer, 2009), pp. 169; D. Yarkony, *J. Chem. Phys.* **123**(13), 134106 (2005); D.R. Yarkony, *J. Chem. Phys.* **123**(20), 204101 (2005).
9. G. Atchity, S. Xantheas and K. Ruedenberg, *J. Chem. Phys.* **95**(3), 1862 (1991).
10. M. Desouter-Lecomte, C. Galloy, J. Lorquet and M. Pires, *J. Chem. Phys.* **71**(9), 3661 (1979); D.R. Yarkony, *Rev. Mod. Phys.* **68**(4), 985 (1996).
11. M.J. Paterson, M.J. Bearpark, M.A. Robb and L. Blancafort, *J. Chem. Phys.* **121**(23), 11562 (2004).
12. M. Paterson, M. Bearpark, M. Robb, L. Blancafort and G. Worth, *Phys. Chem. Chem. Phys.* **7**(10), 2100 (2005).
13. F. Sicilia, L. Blancafort, M.J. Bearpark and M.A. Robb, *J. Chem. Theory Comput.* **4**(2), 257 (2008).
14. B. Lasorne, F. Sicilia, M.J. Bearpark, M.A. Robb, G.A. Worth and L. Blancafort, *J. Chem. Phys.* **128**(12), 124307 (2008).
15. F. Sicilia, L. Blancafort, M.J. Bearpark and M.A. Robb, *J. Phys. Chem.* A **111**(11), 2182 (2007).
16. F. Sicilia, M.J. Bearpark, L. Blancafort and M.A. Robb, *Theor. Chem. Acc.* **118**(1), 241 (2007).
17. B.H. Lengsfield and D.R. Yarkony, *Adv. Chem. Phys.* **82**, 1 (1992).
18. M. Bearpark, M. Robb and H. Schlegel, *Chem. Phys. Lett.* **223**(3), 269 (1994).
19. B.G. Levine, J.D. Coe and T.J. Martinez, *J. Phys. Chem.* B **112**(2), 405 (2008).
20. T.W. Keal, A. Koslowski and W. Thiel, *Theor. Chem. Acc.* **118**(5–6), 837 (2007).

21. G. Worth and L. Cederbaum, *Annu. Rev. Phys. Chem.* **55**, 127 (2004).
22. S. Belz, T. Grohmann and M. Leibscher, *J. Chem. Phys.* **131**(3), 034305 (2009); T. Grohmann, O. Deeb and M. Leibscher, *Chem. Phys.* **338**(2–3), 252 (2007); O. Deeb, S. Cogan and S. Zilberg, *Chem. Phys.* **325**(2), 251 (2006); M. Bearpark, L. Blancafort and M. Paterson, *Mol. Phys.* **104**(5–7), 1033 (2006).
23. M. Olivucci, I. Ragazos, F. Bernardi and M. Robb, *J. Am. Chem. Soc.* **115**(9), 3710 (1993).
24. M. Boggio-Pasqua, M. Bearpark, P. Hunt and M. Robb, *J. Am. Chem. Soc.* **124**(7), 1456 (2002).
25. P. Celani, S. Ottani, M. Olivucci, F. Bernardi and M.A. Robb, *J. Am. Chem. Soc.* **116**(22), 10141 (1994); W. Fuss, T. Schikarski, W.E. Schmid, S. Trushin and K.L. Kompa, *Chem. Phys. Lett.* **262**(6), 675 (1996); W. Fuss, P. Hering, K.L. Kompa, S. Lochbrunner, T. Schikarski, W.E. Schmid and S.A. Trushin, *Ber. Bunsenges. Phys. Chem* **101**(3), 500 (1997); M. Garavelli, P. Celani, M. Fato, M.J. Bearpark, B.R. Smith, M. Olivucci and M.A. Robb, *J. Phys. Chem.* A **101**(11), 2023 (1997); S.A. Trushin, W. Fuss, T. Schikarski, W.E. Schmid and K.L. Kompa, *J. Chem. Phys.* **106**(22), 9386 (1997); A. Hofmann and R. de Vivie-Riedle, *J. Chem. Phys.* **112**(11), 5054 (2000); A. Hofmann and R. de Vivie-Riedle, *Chem. Phys. Lett.* **346**(3–4), 299 (2001); L. Kurtz, A. Hofmann and R. de Vivie-Riedle, *J. Chem. Phys.* **114**(14), 6151 (2001); S. Zilberg and Y. Haas, *Phys. Chem. Chem. Phys.* **4**(1), 34 (2002); H. Tamura, S. Nanbu, H. Nakamura and T. Ishida, *Chem. Phys. Lett.* **401**(4–6), 487 (2005).
26. K. Kosma, S.A. Trushin, W. Fuss and W.E. Schmid, *Phys. Chem. Chem. Phys.* **11**(1), 172 (2009).
27. M. Boggio-Pasqua, M. Ravaglia, M. Bearpark, M. Garavelli and M. Robb, *J. Phys. Chem.* A **107**(50), 11139 (2003).
28. A. Migani, M. Robb and M. Olivucci, *J. Am. Chem. Soc.* **125**(9), 2804 (2003); O. Weingart, A. Migani, M. Olivucci, M. Robb, V. Buss and P. Hunt, *J. Phys. Chem.* A **108**(21), 4685 (2004).
29. I. Gomez, M. Reguero, M. Boggio-Pasqua and M.A. Robb, *J. Am. Chem. Soc.* **127**(19), 7119 (2005).
30. K.A. Zachariasse, S.I. Druzhinin, V.A. Galievsky, S. Kovalenko, T.A. Senyushkina, P. Mayer, M. Noltemeyer, M. Boggio-Pasqua and M.A. Robb, *J. Phys. Chem.* A **113**(12), 2693 (2009).
31. P. Hunt and M. Robb, *J. Am. Chem. Soc.* **127**(15), 5720 (2005).
32. G. Groenhof, M. Bouxin-Cademartory, B. Hess, S. De Visser, H. Berendsen, M. Olivucci, A. Mark and M. Robb, *J. Am. Chem. Soc.* **126**(13), 4228 (2004).
33. L.V. Schaefer, G. Groenhof, A.R. Klingen, G.M. Ullmann, M. Boggio-Pasqua, M.A. Robb and H. Grubmueller, *Angew Chem. Int. Edit.* **46**(4), 530 (2007).
34. M. Paterson, M. Robb, L. Blancafort and A. DeBellis, *J. Phys. Chem.* A **109**(33), 7527 (2005).
35. D. Asturiol, B. Lasorne, M.A. Robb and L. Blancafort, *J. Phys. Chem.* A **113**(38), 10211 (2009).
36. M. Boggio-Pasqua, M.J. Bearpark, F. Ogliaro and M.A. Robb, *J. Am. Chem. Soc.* **128**(32), 10533 (2006).

37. I. Gomez, M. Reguero and M.A. Robb, *J. Phys. Chem.* A **110**(11), 3986 (2006).
38. M. Boggio-Pasqua, M.J. Bearpark and M.A. Robb, *J. Org. Chem.* **72**(12), 4497 (2007).
39. M. Araujo, B. Lasorne, M.J. Bearpark and M.A. Robb, *J. Phys. Chem.* A **112**(33), 7489 (2008).
40. A. Nenov, P. Kolle, M. Robb and R. de Vivie-Riedle, *J. Org. Chem.* **75**, 123 (2010).
41. W.T.A.M. van der Lugt and L.J. Oosterhoff, *J. Am. Chem. Soc.* **91**, 6042 (1969); W.T.A.M. van der Lugt and L.J. Oosterhoff, *Chem. Commun.* 1235–1236 (1968).
42. M.J. Paterson, M.A. Robb, L. Blancafort and A.D. DeBellis, *J. Am. Chem. Soc.* **126**(9), 2912 (2004); A. Migani, L. Blancafort, M.A. Robb and A. D. Debellis, *J. Am. Chem. Soc.* **130**(22), 6932 (2008).
43. G. Groenhof, L.V. Schaefer, M. Boggio-Pasqua, M. Goette, H. Grubmueller and M.A. Robb, *J. Am. Chem. Soc.* **129**(21), 6812 (2007).
44. Y. Haas and S. Zilberg, *Adv. Chem. Phys.* **124**, 433 (2002); Y. Haas, S. Cogan and S. Zilberg, *Int. J. Quantum Chem.* **102**(5), 961 (2005).
45. S. Vanni, M. Garavelli and M.A. Robb, *Chem. Phys.* **347**(1–3), 46 (2008).
46. B. Dick, Y. Haas and S. Zilberg, *Chem. Phys.* **347**(1–3), 65 (2008).
47. M. Abe, Y. Ohtsuki, Y. Fujimura, Z.G. Lan and W. Domcke, *J. Chem. Phys.* **124**(22), 224316 (2006); S. Althorpe, *J. Chem. Phys.* **124**(8), 084105 (2006).
48. H.C. Longuet–Higgins, *Proc. Roy. Soc. London* A **392**, 147 (1975).
49. S.C. Althorpe, *J. Chem. Phys.* **124**(8), 084105 (2006).
50. F. Bernardi, M. Olivucci, M. Robb and G. Tonachini, *J. Am. Chem. Soc.* **114**(14), 5805 (1992).
51. D.S. Ruiz, A. Cembran, M. Garavelli, M. Olivucci and W. Fuss, *Photochem Photobiol* **76**(6), 622 (2002).
52. I. Palmer, I. Ragazos, F. Bernardi, M. Olivucci and M. Robb, *J. Am. Chem. Soc.* **115**(2), 673 (1993).
53. S. Zilberg and Y. Haas, *Chem. Eur. J.* **5**(6), 1755 (1999).
54. G. Worth and M. Robb, *Adv. Chem. Phys.* **124**, 355 (2002); M.D. Hack, A.M. Wensmann, D.G. Truhlar, M. Ben-Nun and T.J. Martinez, *J. Chem. Phys.* **115**(3), 1172 (2001); J. Quenneville, M. Ben-Nun and T.J. Martinez, *J. Photoch. Photobio.* A **144**(2–3), 229 (2001); A. Jasper, S. Nangia, C. Zhu and D. Truhlar, *Accounts Chem. Res.* **39**(2), 101 (2006); M. Barbatti, G. Granucci, M. Persico, M. Ruckenbauer, M. Vazdar, M. Eckert-Maksic and H. Lischka, *J. Photoch. Photobio.* A **190**(2–3), 228 (2007).
55. A. Sanchez-Galvez, P. Hunt, M. Robb, M. Olivucci, T. Vreven and H. Schlegel, *J. Am. Chem. Soc.* **122**(12), 2911 (2000).
56. B. Dietzek, B. Brueggemann, P. Persson and A. Yartsev, *Chem. Phys. Lett.* **455**(1–3), 13 (2008).
57. I.J. Palmer, M. Olivucci, F. Bernardi and M.A. Robb, *J. Org. Chem.* **57**(19), 5081 (1992); W. Domcke, A. Sobolewski and C. Woywod, *Chem. Phys. Lett.* **203**(2–3), 220 (1993).
58. W. Domcke, A.L. Sobolewski and C. Woywod, *Chem. Phys. Lett.* **203**(2–3), 220 (1993); H. Koppel, *Chem. Phys. Lett.* **205**(4–5), 361 (1993); I.J. Palmer,

I.N. Ragazos, F. Bernardi, M. Olivucci and M.A. Robb, *J. Am. Chem. Soc.* **115**(2), 673 (1993); A. Sobolewski, C. Woywod and W. Domcke, *J. Chem. Phys.* **98**(7), 5627 (1993); B.R. Smith, M.J. Bearpark, M.A. Robb, F. Bernardi and M. Olivucci, *Chem. Phys. Lett.* **242**(1–2), 27 (1995); G.A. Worth, *J. Photoch Photobio* A **190**(2–3), 190 (2007).

59. B. Lasorne, M.J. Bearpark, M.A. Robb and G.A. Worth, *J. Phys. Chem.* A **112**(50), 13017 (2008).
60. B. Lasorne, M.A. Robb and G.A. Worth, Phys. *Chem. Chem. Phys.* **9**(25), 3210 (2007); B. Lasorne, M.J. Bearpark, M.A. Robb and G.A. Worth, *Chem. Phys. Lett.* **432**(4–6), 604 (2006).
61. G. Groenhof, L.V. Schaefer, M. Boggio-Pasqua, H. Grubmueller and M.A. Robb, *J. Am. Chem. Soc.* **130**(11), 3250 (2008).
62. A. Strambi, P.B. Coto, L.M. Frutos, N. Ferre and M. Olivucci, *J. Am. Chem. Soc.* **130**(11), 3382 (2008); P.B. Coto, A. Strambi and M. Olivucci, *Chem. Phys.* **347**(1–3), 483 (2008); F. Santoro, A. Lami and M. Olivucci, *Theor. Chem. Acc.* **117**(5–6), 1061 (2007); A.M. Virshup, C. Punwong, T.V. Pogorelov, B.A. Lindquist, C. Ko and T.J. Martinez, *J. Phys. Chem.* B **113**(11), 3280 (2009).
63. H.R. Hudock, H.G. Levine, A.L. Thompson and T.J. Martinez, presented at the International Conference on Computational Methods in Science and Engineering, Corfu, Greece, 2007 (unpublished); M. Boggio-Pasqua, G. Groenhof, L.V. Schafer, H. Grubmuller and M.A. Robb, *J. Am. Chem. Soc.* **129**(36), 10996 (2007); G. Groenhof, L.V. Schafer, M. Boggio-Pasqua, M. Goette, H. Grubmuller and M.A. Robb, *J. Am. Chem. Soc.* **129**(21), 6812 (2007).
64. G. Villani, *J. Chem. Phys.* **128**(11), 114306 (2008); T. Rozgonyi and L. Gonzalez, *J. Phys. Chem.* A **112**(25), 5573 (2008); M. Basler, E. Gindensperger, H. D. Meyer and L.S. Cederbaum, *Chem. Phys.* **347**(1–3), 78 (2008); B.G. Levine, J.D. Coe, A.M. Virshup and T.J. Martinez, *Chem. Phys.* **347**(1–3), 3 (2008).
65. D. Geppert, P. von den Hoff and R. de Vivie-Riedle, *J. Phys. B-At Mol. Opt.* **41**(7), 074006 (2008); J. Hauer, T. Buckup and M. Motzkus, *J. Phys. Chem.* A **111**(42), 10517 (2007); P.S. Christopher, M. Shapiro and P. Brumer, *J. Chem. Phys.* **123**(6), 064313 (2005); M. Abe, Y. Ohtsuki, Y. Fujimura and W. Domcke, *J. Chem. Phys.* **123**(14), 144508 (2005); A. Muller and K. Kompa, *J. Mod. Optic.* **49**(3–4), 627 (2002).
66. L.M. Frutos, T. Andruniow, F. Santoro, N. Ferre and M. Olivucci, *Proc. Natl. Acad. Sci. U.S.A.* **104**(19), 7764 (2007); L.V. Schafer, G. Groenhof, M. Boggio-Pasqua, M.A. Robb and H. Grubmuller, *Plos. Comput. Biol.* **4**(3), 14 (2008); L.V. Schaefer, G. Groenhof, M. Boggio-Pasqua, M.A. Robb and H. Grubmueller, *Plos. Comput. Biol.* **4**(3), e1000034 (2008).
67. M.A. Robb, M. Garavelli, M. Olivucci and F. Bernardi, in *Reviews in Computational Chemistry,* **15**, 87 (2000).